

UNIVERSITY OF WEST BOHEMIA
IN PILSEN
FACULTY OF APPLIED SCIENCES
DEPARTMENT OF MECHANICS

DIPLOMA THESIS

**MATERIAL PARAMETERS IDENTIFICATION OF
RHEOLOGICAL MODEL OF RUBBER MATRIX
COMPOSITE**

Pilsen 2016

Bc. Jiří Kocáb

ZADÁNÍ DIPLOMOVÉ PRÁCE

(PROJEKTU, UMĚLECKÉHO DÍLA, UMĚLECKÉHO VÝKONU)

Jméno a příjmení: **Bc. Jiří KOCÁB**
Osobní číslo: **A14N0183P**
Studijní program: **N3955 Počítačové modelování v inženýrství**
Studijní obor: **Aplikovaná mechanika**
Název tématu: **Identifikace materiálových parametrů modelu reologického chování kompozitu s pryžovou maticí**
Zadávací katedra: **Katedra mechaniky**

Z á s a d y p r o v y p r a c o v á n í :

1. Provést rešerši modelů reologického chování.
2. Experimentálně vyšetřit mechanické vlastnosti kompozitu s pryžovou maticí.
3. Vybrat model, který je schopný vystihnout vyšetřené mechanické vlastnosti s přijatelnou přesností.
4. Identifikovat materiálové parametry.
5. Vymezit platnost vybraného modelu a identifikovaných parametrů.
6. Pomocí numerických simulací vybraných experimentů demonstrovat dosaženou shodu modelu s reálných chováním kompozitu.

Rozsah grafických prací:

Rozsah kvalifikační práce: **40-60 stran A4 včetně příloh**

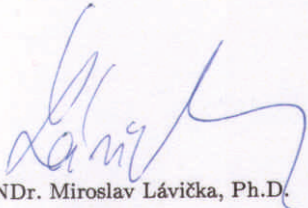
Forma zpracování diplomové práce: **tištěná**

Seznam odborné literatury:

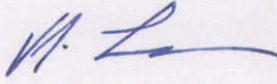
1. Doghri, I: **Mechanics of Deformable Solids**. Springer, 2000.
2. Gil-Negrete, N., Alonso, A.: **Constitutive Models for Rubber VIII**. 2013.
3. Hosford, W. F.: **Solid Mechanics**. 2010.
4. Simo, J. C., Hughes, T. J. R.: **Computational Inelasticity**. 1998.
5. de Souza Neto, E.A., Peric, D., Owen, D. R. J.: **Computational Methods for Plasticity: Theory and Applications**. John Wiley & Sons, Ltd, 2008.

Vedoucí diplomové práce: **Ing. Radek Kottner, Ph.D.**
Katedra mechaniky

Datum zadání diplomové práce: **8. října 2015**
Termín odevzdání diplomové práce: **31. května 2016**


Doc. RNDr. Miroslav Lávička, Ph.D.
děkan




Prof. Ing. Vladislav Laš, CSc.
vedoucí katedry

V Plzni dne 8. října 2015

Declaration

I hereby certify that this diploma thesis is entirely the result of my work and I faithfully and properly cited all sources used in the thesis.

In Pilsen, 31.5.2016

Jiří Kocáb

Abstract

This thesis deals with material parameters calibration of a cork-rubber composite Amorim ACM87, whose mechanical behaviour is similar to rubbers. In order to calibrate (identify) material parameters, mechanical experiments were performed and corresponding numerical simulations were performed using finite element based software Abaqus. The behaviour of given material was investigated for different strain rates and loading modes. Material parameters were calibrated using numerical optimisation methods driven by optimisation software optiSLang. The difference between the results of experiments and numerical simulations was compared and minimized. The Parallel network model with three viscoelastic networks and Mullins effect was chosen as a material model.

Abstrakt

Tato práce se zabývá identifikací materiálových parametrů korkového kompozitu Amorim ACM87, jehož mechanické vlastnosti jsou velice podobné pryžím. Aby bylo možné identifikovat materiálové parametry, byla provedena série experimentů pro různé módy a rychlosti zatěžování. Dále byly provedeny numerické simulace pomocí programu Abaqus, založeného na metodě konečných prvků. Materiálové parametry byly identifikovány pomocí metod numerické optimalizace, která byla provedená pomocí optimalizačního software optiSLang. Rozdíl mezi výsledky měření a numerických simulací byl porovnáván a minimalizován. Jako materiálový model byl použit Parallel network model se třemi viskoelastickými větvemi a Mullinsovým efektem.

Acknowledgements

I would like to thank my supervisor, Ing. Radek Kottner, Ph.D for his support and encouragement while writing my diploma thesis. My special thanks go to Ing. Jan Krystek, Ph.D for helping me with experiments, M.Sc Attila Kossa, Ph.D, for helpful pieces of advice during my study period in Budapest and Bc. Martin Berka for English language revision. I would also like to thank my family and friends for supporting me during my studies.

Contents

1	Introduction	1
1.1	Software background	2
2	State of art	3
3	Experiments	5
3.1	Performed experiments	7
3.2	Loading history	8
3.3	Results of experiments	9
4	Material models	16
4.1	Elasticity	16
4.2	Hyperelasticity	17
4.2.1	Constitutive equations	17
4.2.2	Decoupled Formulation	19
4.2.3	Hyperelastic material models	19
4.3	Strain softening	22
4.4	Viscoelasticity	23
4.4.1	Small strain linear viscoelasticity	23
4.4.2	Large strain linear viscoelasticity	24
4.4.3	Prony series	25
4.5	Parallel network model	25
4.5.1	Elastic response	26
4.5.2	Viscous response	27
4.5.3	Mullins effect	28
4.5.4	PN model in Abaqus	29
5	Material parameters calibration	31
5.1	Numerical simulations	31
5.1.1	Uniaxial tension	32
5.1.2	Uniaxial compression	33
5.1.3	Simple shear	34
5.1.4	Material model	36
5.2	Numerical Optimization	36

5.2.1	Evolution algorithms	37
5.2.2	Gradient based algorithm	38
5.3	Objective function	38
5.4	Optimization task	41
5.5	Cork-rubber parameters calibration	41
5.5.1	Calibration for combination of tension and shear	43
6	Results	46
7	Conclusion	57

List of Figures

3.1	Experiments with the directions of loads highlighted: (a) uniaxial tension, (b) uniaxial compression, (c) simple shear, (d) volumetric test.	5
3.2	Cork-rubber composite samples	6
3.3	Loading history of experiments	8
3.4	Volumetric compression, strain rate 0.02 s^{-1}	9
3.5	Force-Displacement diagram: simple tension samples	10
3.6	Force-time diagram: simple tension sample, strain rate 1 s^{-1}	10
3.7	Force-time diagram: simple tension sample, strain rate 0.1 s^{-1}	11
3.8	Force-time diagram: simple tension sample, strain rate 0.01 s^{-1}	11
3.9	Force-Displacement diagram: simple compression samples	12
3.10	Force-time diagram: simple compression sample, strain rate 1 s^{-1}	12
3.11	Force-time diagram: simple compression sample, strain rate 0.1 s^{-1}	13
3.12	Force-time diagram: simple compression sample, strain rate 0.01 s^{-1}	13
3.13	Force-Displacement diagram: shear samples	14
3.14	Force-time diagram: shear sample, strain rate 1 s^{-1}	14
3.15	Force-time diagram: shear sample, strain rate 0.1 s^{-1}	15
3.16	Force-time diagram: shear sample, strain rate 0.01 s^{-1}	15
4.1	Stress-strain relationships for: (a) linear elastic material, (b) non-linear elastic material, (c) viscoelastic material [20].	17
4.2	Representation of 8 chain model in (a) undeformed, (b) uniaxial extension and (c) biaxial extension configurations [6].	22
4.3	Response of viscoelastic material: (a) loading a unloading, (b) different strain rate stretching [21]	23
4.4	Schemes of viscoelastic models (a) Maxwell model, (b) Voight model and (c) standard linear solid model	24
4.5	Schemes of the Prony series	25
4.6	Scheme of PNM	26
5.1	Boundary conditions of tension model	32
5.2	Boundary conditions and mesh of uniaxial compression finite element model	34
5.3	Boundary conditions and mesh of simple shear finite element model . . .	35
5.4	Scheme of evolution algorithms [13]	38
5.5	Comparison of predicted and experimental data	39

5.6	Time-force diagram with relaxation parts highlighted	40
5.7	Diagram of the optimisation task	41
5.8	Uniaxial compression simulation errors	42
5.9	Scheme of the optimisation procedure	45
6.1	Comparison of experimental and predicted data for calibrated parameters: force-time diagram, uniaxial tension, strain rate 1 s^{-1}	48
6.2	Comparison of experimental and predicted data for calibrated parameters: force-displacement diagram, uniaxial tension, strain rate 1 s^{-1}	48
6.3	Comparison of experimental and predicted data for calibrated parameters: force-time diagram, uniaxial tension, strain rate 0.1 s^{-1}	49
6.4	Comparison of experimental and predicted data for calibrated parameters: force-displacement diagram, uniaxial tension, strain rate 0.1 s^{-1}	49
6.5	Comparison of experimental and predicted data for calibrated parameters: force-time diagram, uniaxial tension, strain rate 0.01 s^{-1}	50
6.6	Comparison of experimental and predicted data for calibrated parameters: force-displacement diagram, uniaxial tension, strain rate 0.01 s^{-1}	50
6.7	Comparison of experimental and predicted data for calibrated parameters: force-time diagram, simple shear, strain rate 1 s^{-1}	51
6.8	Comparison of experimental and predicted data for calibrated parameters: force-displacement diagram, simple shear, strain rate 1 s^{-1}	51
6.9	Comparison of experimental and predicted data for calibrated parameters: force-time diagram, simple shear, strain rate 0.1 s^{-1}	52
6.10	Comparison of experimental and predicted data for calibrated parameters: force-displacement diagram, simple shear, strain rate 0.1 s^{-1}	52
6.11	Comparison of experimental and predicted data for calibrated parameters: force-time diagram, simple shear, strain rate 0.01 s^{-1}	53
6.12	Comparison of experimental and predicted data for calibrated parameters: force-displacement diagram, simple shear, strain rate 0.01 s^{-1}	53
6.13	Comparison of experimental and predicted data for calibrated parameters: force-time diagram, uniaxial compression, strain rate 1 s^{-1}	54
6.14	Comparison of experimental and predicted data for calibrated parameters: force-displacement diagram, uniaxial compression, strain rate 1 s^{-1}	54
6.15	Comparison of experimental and predicted data for calibrated parameters: force-time diagram, uniaxial compression, strain rate 0.1 s^{-1}	55
6.16	Comparison of experimental and predicted data for calibrated parameters: force-displacement diagram, uniaxial compression, strain rate 0.1 s^{-1}	55
6.17	Comparison of experimental and predicted data for calibrated parameters: force-time diagram, uniaxial compression, strain rate 0.01 s^{-1}	56

6.18 Comparison of experimental and predicted data for calibrated parameters:
force-displacement diagram, uniaxial compression, strain rate 0.01 s^{-1} . . 56

List of Tables

3.1	Parameters of performed experiments	6
4.1	Viscous evolution law definition	30
5.1	Used material model	36
5.2	Parameters with initial values and boundaries for the global evolution algorithm	44
5.3	Parameters with initial values and boundaries for the local evolution and gradient algorithm	44
5.4	Parameters of algorithms	45
6.1	Results of material parameter calibration for combination of tension and shear	47

List of Symbols

δ	-	Kronecker delta
$\dot{\varepsilon}$	s^{-1}	Strain rate
ε	-	Engineering strain
$\lambda_1, \lambda_2, \lambda_3$	-	Principal stretches
$\overline{\lambda}_1, \overline{\lambda}_2, \overline{\lambda}_3$	-	Modified principal stretches
μ_0	Nm^{-2}	Initial shear modulus
$\boldsymbol{\sigma}$	-	Cauchy stress tensor
σ	Nm^{-2}	Engineering stress
τ_i	s	Relaxation time
$\boldsymbol{\tau}$	-	Kirchhoff stress tensor
$\mathbf{C}, \dot{\mathbf{C}}$	-	Right Cauchy-Green deformation tensor / rate of deformation tensor
$\overline{\mathbf{C}}$	-	Modified Cauchy-Green deformation tensor
\mathbf{d}	-	Rate of deformation tensor
E_R	Nm^{-2}	Relaxation modulus
$\mathbf{E}, \dot{\mathbf{E}}$	-	Green-Lagrange deformation tensor / rate of deformation tensor
F	N	Force
\mathbf{F}	-	Deformation gradient
$\dot{\mathbf{F}}$	-	The rate of change of deformation gradient
\mathbf{F}^e	-	Elastic part of deformation gradient
\mathbf{F}^{pl}	-	Plastic part of deformation gradient
\mathbf{F}_{cr}	-	Creep part of deformation gradient
\mathbf{F}_{vol}	-	Volumetric part of deformation gradient
\mathbf{F}_{iso}	-	Isochoric part of deformation gradient
g_R	-	Normalised relaxation modulus
I_1, I_2, I_3	-	Principal invariants
$\overline{I}_1, \overline{I}_2, \overline{I}_3$	-	Modified principal invariants
J	-	Volume ratio
k	J/K	Boltzmann constant
K	Nm^{-2}	Bulk modulus
K_0	Nm^{-2}	Initial Bulk modulus
l	m	length
l_0	mm	Reference length

P	-	First Piola-Kirchhoff stress tensor
S	-	Second Piola-Kirchhoff stress tensor
<i>t</i>	s	Time
<i>W</i>	Jm^{-3}	Strain energy density
\dot{W}	$Jm^{-3}s^{-1}$	Rate of change of W
W_{iso}	Jm^{-3}	isochoric part of strain energy density
W_{vol}	Jm^{-3}	volumetric part of strain energy density

Following symbols: $a, A, B, C, E, D, m, n, r, q_0, \alpha_i, \beta, \dot{\epsilon}, \mu_i, \lambda_m$ are material parameters described in chapter 4.

1 Introduction

Cork is a natural material with exceptional properties and large number of applications. Low weight, elasticity, flexibility and insulation properties make the cork a very valued raw material. Bottle stoppers were for a long time the main product of cork, however 25% of raw material at most can be utilised during cork stoppers production. Around 75% of raw material was a worthless waste [15]. At the beginning of 19th the methods of cork agglomerates production were invented. Since this moment, the waste of cork stoppers production have became very valuable. These days, cork or its agglomerates are used as floor coverings, thermal or acoustic insulation and energy absorbing material. Cork agglomerates can be divided into two basic groups: insulation corkboard and composition cork. Insulation corkboard consists only of cork without any additives, thus it can't be labeled as a composite material. Composition cork is made from cork particles bonded together using different binders [15]. This thesis deals with cork composite Amorim ACM87 from a group of composition cork. The composite consists of cork particles bonded together using rubber. Mechanical properties of cork rubber composites are similar to rubbers, but cork particles come from renewable sources, which makes these products more environmentally friendly.

Following thesis deals with the cork composite material parameters calibration, which is very complicated task consisting of several steps. First of all, the mechanical behaviour of given material has to be investigated. A series of experiments with different loading modes and strain rates will be performed. According to results of the experiments, a suitable material model will be chosen. Material models suitable for the cork composite will be researched. Parameters of chosen model will be calibrated using a numerical optimisation, where the difference between results of the experiments and results of numerical simulations (predictions) will be minimized. The last step is to identify the region of validity of calibrated parameters and demonstrate the results.

Material models suitable for rubber-like materials are much more complicated in comparison to material models usually used for steel. Elastic behaviour of steel can be described for small strains using Hook's law and two material parameters. Behaviour of rubber-like materials is not purely elastic, but more complex, consisting of viscoelastic, viscoplastic and other behaviours. Each of this behaviour can be modelled using appropriate material model with given parameters. The more parameter is calibrated the more complicated the task is.

1.1 Software background

Numerical simulations will be performed using Abaqus 6.14, which is a finite element based computation software. Abaqus provides many material models including a Parallel network model, which is one of the most advanced material models used for rubber-like materials modelling. Material models listed in chapter 4 are chosen with respect to used software. As a tool for numerical optimisation, the optiSLang 4.2 software will be used. This software is suitable for sensitivity analysis, multiobjective and multidisciplinary optimisation. Both software products are available at the Department of Mechanics at the University of West Bohemia in Pilsen. Numerical models definition and the processing of results will be performed using Python scripts.

2 State of art

Cork composite Amorim ACM87 can be classified as a rubber-like material with mechanical behaviour similar to rubbers. Cork-composite research at The University of West Bohemia has been started by [24], where the cork-composite ACM87 was used as a damping layer for carbon fibre reinforced plastics. In bachelor thesis [22], the material behaviour up to 25 % nominal strains was investigated, without considering the strain rate effect and cyclic loading. Material parameters were successfully calibrated for the combination of uniaxial tension and uniaxial compression using optiSLang. In case of simple shear was the prediction of material behaviour very inaccurate for the calibrated parameters. The chosen material model consisted of Prony series and hyperelastic generalised polynomial model of third order.

The modelling of cork-rubber composites is not so common as modelling of rubber-like materials, but the same isotropic material models can be used. The most common way to predict the behaviour of rubber-like materials is by using the linear viscoelasticity theory. For linear viscoelasticity is the time dependent shear modulus of the material independent of stress magnitude [25]. Linear viscoelasticity approach is suitable for small strains and for materials with low strain rate effect. As a model for linear elasticity, the Prony series is usually used. For example in [14], the process of material parameter identification of rubber compound used for tires production was described. Series of uniaxial tension experiments for one strain rate were performed and material parameters of viscoelastic model were successfully calibrated. Material model was chosen as a combination of the Prony series and a hyperelastic model. Three hyperelastic models were investigated: Ogden, Yeoh and polynomial. The material parameter calibration was performed using Abaqus.

A new group of material models suitable for modelling of rubber-like materials are viscoplastic material models. These models are designed to predict non-linear viscoelastic or viscoplastic behaviour with high accuracy. The most known viscoplastic models are Bergstrom-Boyce model, Parallel network model and Three network model. In [25], the behaviour of tires was investigated and simulated. Series of tension stress relaxation experiments were performed for 30%, 50%, 70% and 90% strain. During these experiments, the samples were loaded by constant strain and the force response was measured. Based on the experiments, the material parameters of linear viscoelastic model and non-linear

viscoelastic model were calibrated. Linear viscoelastic model consisted of Prony series with Yeoh hyperelastic model. The Parallel network model formed by 3 viscoelastic networks was used as a Non-linear viscoelastic model. Material parameter calibration was done using Isight 5.8. The Parallel network model was implemented in Abaqus in year 2012. One of the first published works that dealt with non-linear viscoelasticity / viscoplasticity in Abaqus was published in [18]. In this work the Parallel network model was introduced and material parameters of ABS plastics were identified using Isight. Performed stress relaxation experiments were designed for up to 2,5% strains without considering the strain rate effect. In this case, axial and torsional loading of the sample were investigated.

A large number of viscoplastic models are listed in [9], where results and errors of material parameter calibration for different material models are shown. However, most of the listed material models are not implemented in finite elements programs. Company Veryst engineering offers material models library PolyUMod [4], which provides advanced material models. PolyUmod is available for almost all FE programs. Veryst engineering offers material parameter extraction software MCalibration, which is able to calibrate any PolyUmod, Abaqus and other material models, based on available experimental data. This software is the most advanced way of identifying material parameters of rubber-like materials or biomaterials.

Material models suitable for rubber-like materials will be discussed in chapter 4.

3 Experiments

For the purpose of proper identification of the cork-composite behaviour, 4 types of experiments were performed. When performing polymer viscoelastic materials testing and modeling, it is very important to perform experiments with different strain-rates and for different loading modes. Loading history and strain-rates were taken from J.Bergstrom's website PolymerFem [8], which is focused on polymer materials testing and modeling. In Figure 3.1 are shown chosen loading modes: uniaxial tension (a), uniaxial compression (b), simple shear (c) and volumetric test (d).

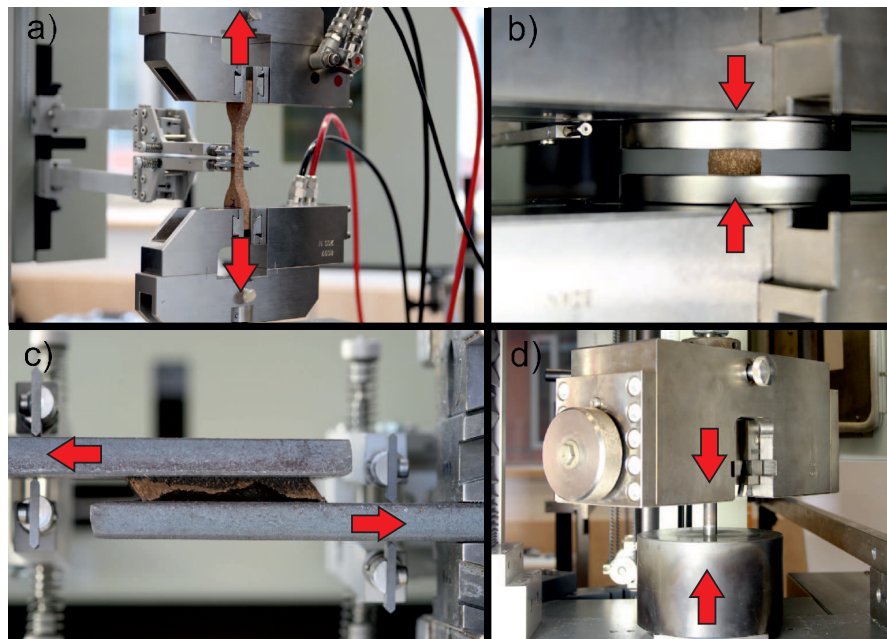


Figure 3.1: Experiments with the directions of loads highlighted: (a) uniaxial tension, (b) uniaxial compression, (c) simple shear, (d) volumetric test.

Table 3.1: Parameters of performed experiments

Loading mode	Strain rate [s^{-1}]	Relax. time t_r [s]	reference length l_0 [mm]
Tension	0.01	60	10
Tension	0.1	60	10
Tension	1	60	10
Compression	0.01	60	9
Compression	0.1	60	9
Compression	1	60	9
Shear	0.01	60	6
Shear	0.1	60	6
Shear	1	60	6
Volumetric test	0.02	0	9

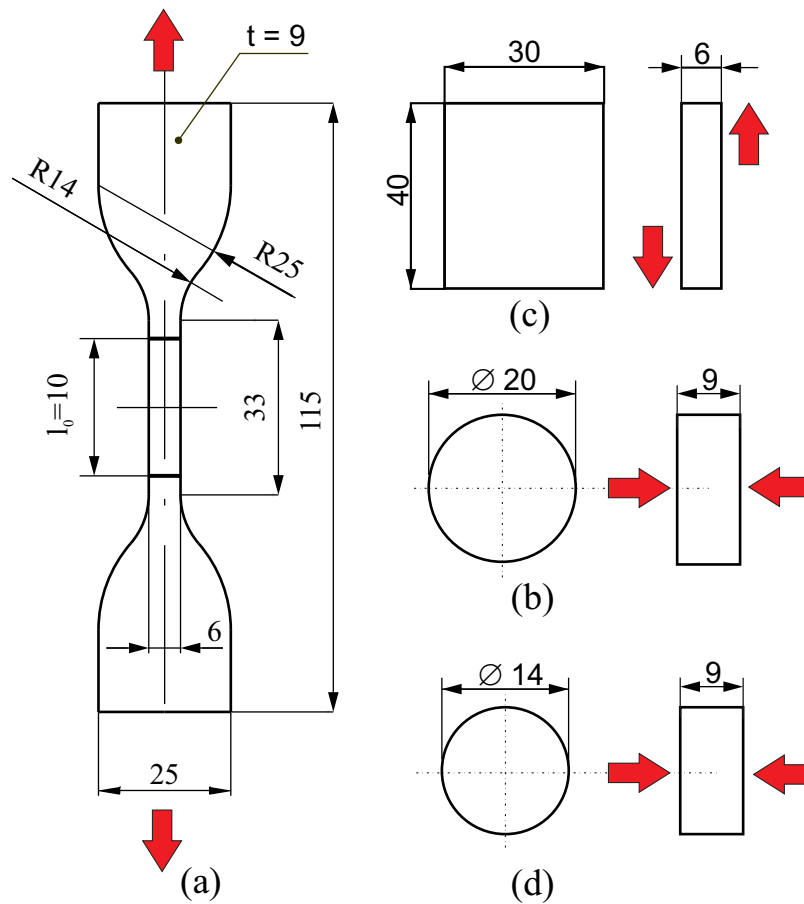


Figure 3.2: Cork-rubber composite samples

3.1 Performed experiments

The cork-rubber composite Amorim ACM87 is available in plates of various thickness. Samples used in these experiments were cut using water jet from plates 6 and 9 mm thick. Dimensions and shapes of samples are partly taken from [10] with respect to available material. Figures 3.1 and 3.2 show performed experiments and samples with directions of loading. Following part describes the performed experiments.

Experiments were performed on Zwick/Roell Z050 testing machine using 200 N and 50 kN load cells. A contact-type extensometer with two sensor arms was used to measure displacements. Loading was controlled by a displacement, to provide stress relaxation experiments. Time, displacement and reaction force was measured with sampling frequency 50 Hz.

Uniaxial tension

The dog bone sample was used for uniaxial tensions experiment. This shape provides uniform stress and strain distribution in central section and minimizes the influence of clamping of the sample. Central section of initial length l_0 is shown in Figure 3.2 (a). Displacement of the central section was measured by mechanical extensometer to provide more accurate results.

Uniaxial compression

The uniaxial compression experiment was performed using two steel plates mounted on the experimental machine as shown in 3.1 (b). The sample of cork-rubber composite was placed between these plates and load was applied. During loading, a bulging of the sample can be observed. This bulging is caused by friction between the steel plates and the sample. The displacement of upper metal plate was measured and the lower metal plate was fixed.

Simple shear

The simple shear was performed using 2 steel plates as shown in Figure 3.1 (c). Cork-composite sample was glued to steel plates using Loctite 480. Metal plates were mounted

into the testing machine and loaded. The displacement of the steel plates was measured.

Volumetric test

In order to identify compressibility of cork-rubber composite, volumetric test according ASTM standards [5] was performed. The sample was placed into a steel vessel of inner diameter equal to diameter of the sample and was loaded using steel rod of the same diameter, as shown in Figure 3.1 (d). Displacement of the steel rod was measured.

3.2 Loading history

In accordance with [8], tests with stress relaxation parts were chosen, which allows us to observe viscoelastic behaviour of cork-composite. Stress relaxation means that sample is loaded by constant strain and stress (force) response is observed.

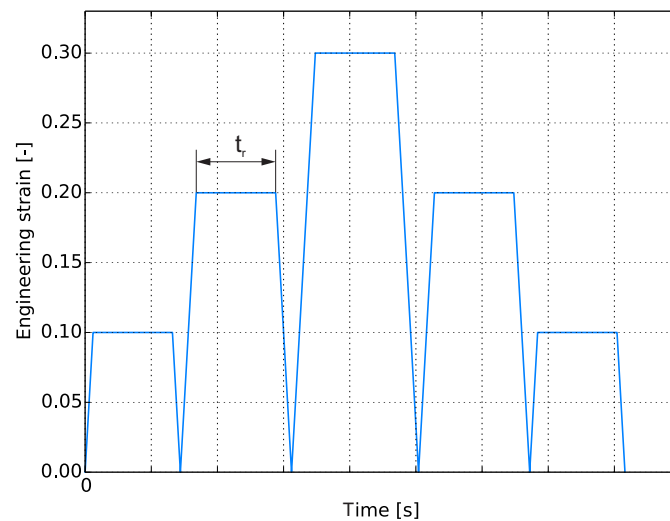


Figure 3.3: Loading history of experiments

Loading history of uniaxial tension, uniaxial compression and simple shear are shown in Figure 3.3, where t_r is the relaxation time, which was set to 60 s. Strain rates $\dot{\epsilon}$ were chosen as 0.01 s^{-1} , 0.1 s^{-1} and 1 s^{-1} to identify behaviour of material in different strain rates. Levels of engineering strain were 10%, 20% and 30%. The strain rate of the volumetric test was 0.02 s^{-1} and 3 loading cycles up to 30% of engineering strain without relaxation were performed. Engineering strain and strain rate was related to reference length l_0 , which is listed in Table 3.1.

3.3 Results of experiments

Following force-displacement and time-displacement diagrams (Figures 3.5-3.16) show results of performed experiments, letters in the legend represent the mode of loading (**T**ension, **C**ompression, **S**hear or **V**olumetric test) and the number represents the strain rate $\dot{\epsilon}$ [s^{-1}]. Each experiment was performed on three samples from which the representative sample was chosen and its results are shown.

It is evident from Figures 3.5, 3.9 and 3.13 that the material response is viscoelastic and strongly rate dependent. Loading and unloading curves are not coincident and form a hysteresis curve. Loading and unloading curves of different strain rates have a similar shape, but a significant difference in reaction force can be observed. The greater the strain rate, the greater the reaction force.

Relaxation parts of experiments can be better seen in Figures 3.6 - 3.8, 3.10 - 3.12 and 3.14 - 3.16. A decrease of the reaction force during the relaxation depends on the strain rate. The greater the strain rate, the greater the decrease. The material softening can be observed in the same Figures.

Figure 3.4 shows the results of volumetric compression test. Arrows indicate loading and unloading curves of the appropriate cycle. The initial bulk modulus $K_0 = 9.3 \times 10^6 \text{ Nm}^{-2}$ was determined by assuming hydrostatic stress field.

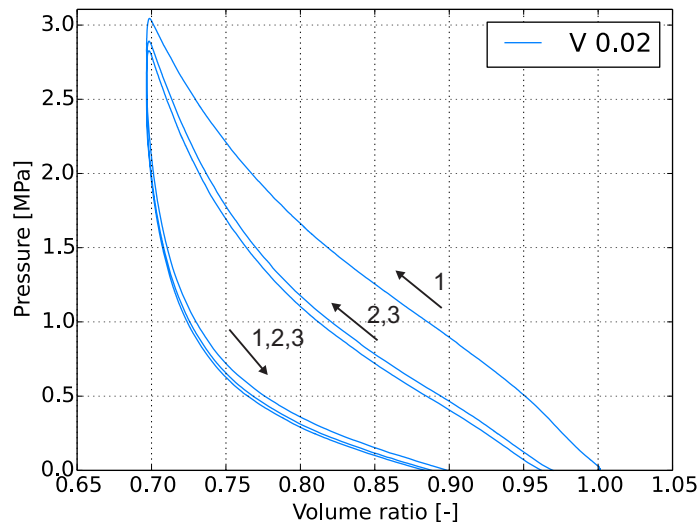


Figure 3.4: Volumetric compression, strain rate 0.02 s^{-1} .

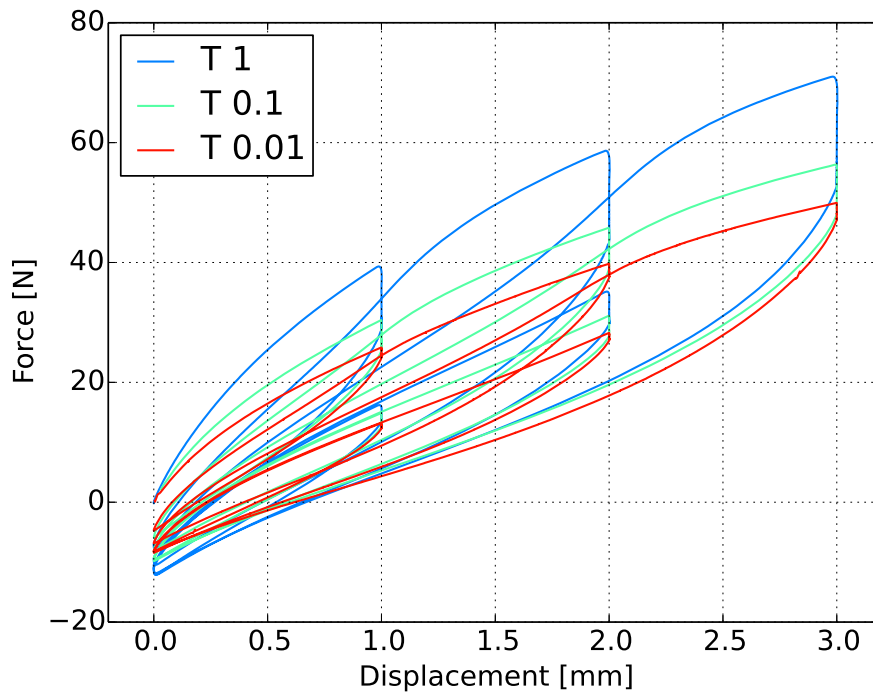
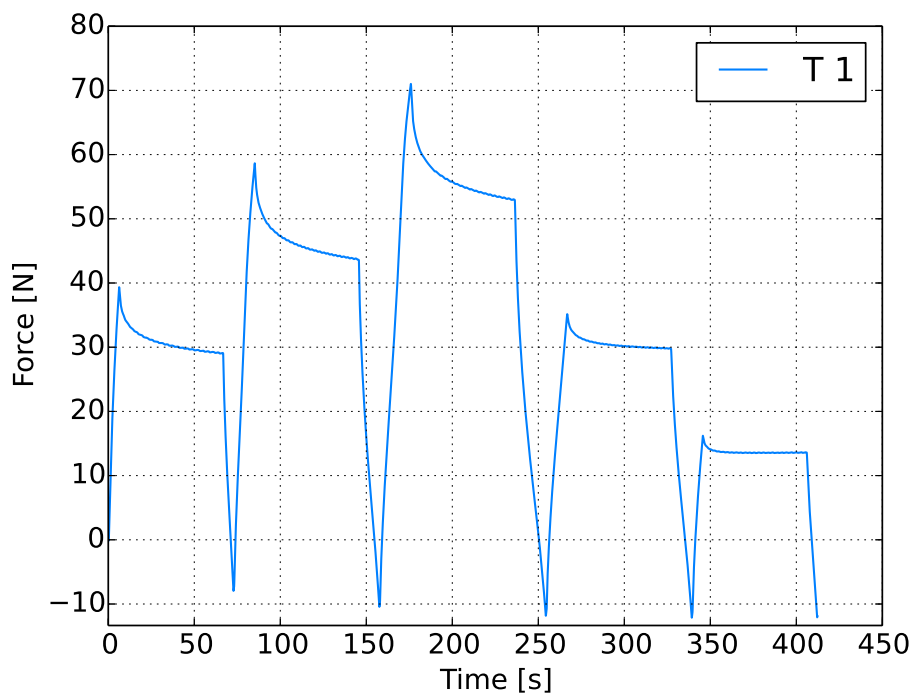


Figure 3.5: Force-Displacement diagram: simple tension samples

Figure 3.6: Force-time diagram: simple tension sample, strain rate 1 s^{-1} .

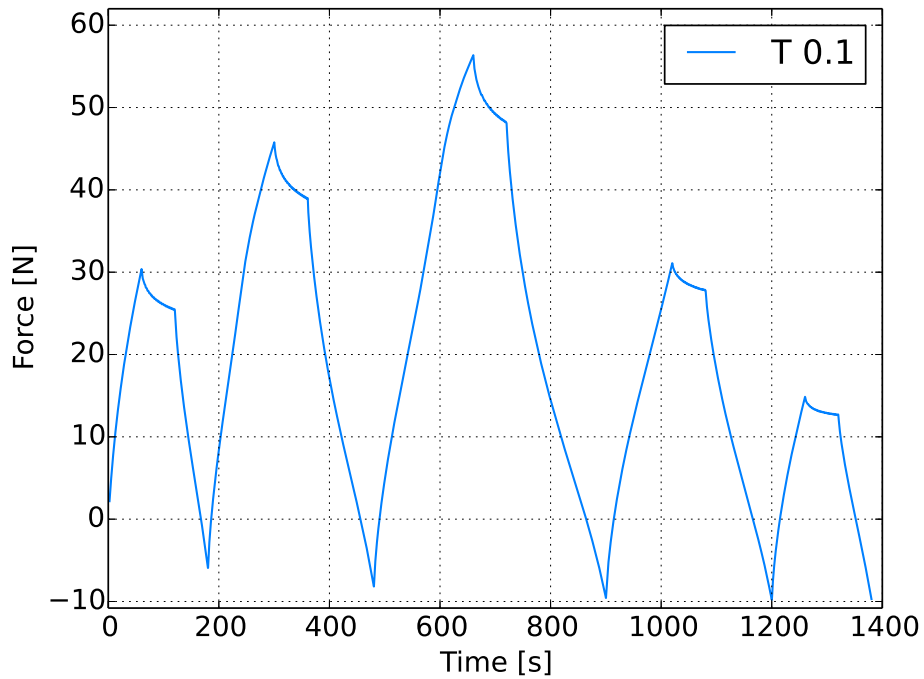


Figure 3.7: Force-time diagram: simple tension sample, strain rate 0.1 s^{-1} .

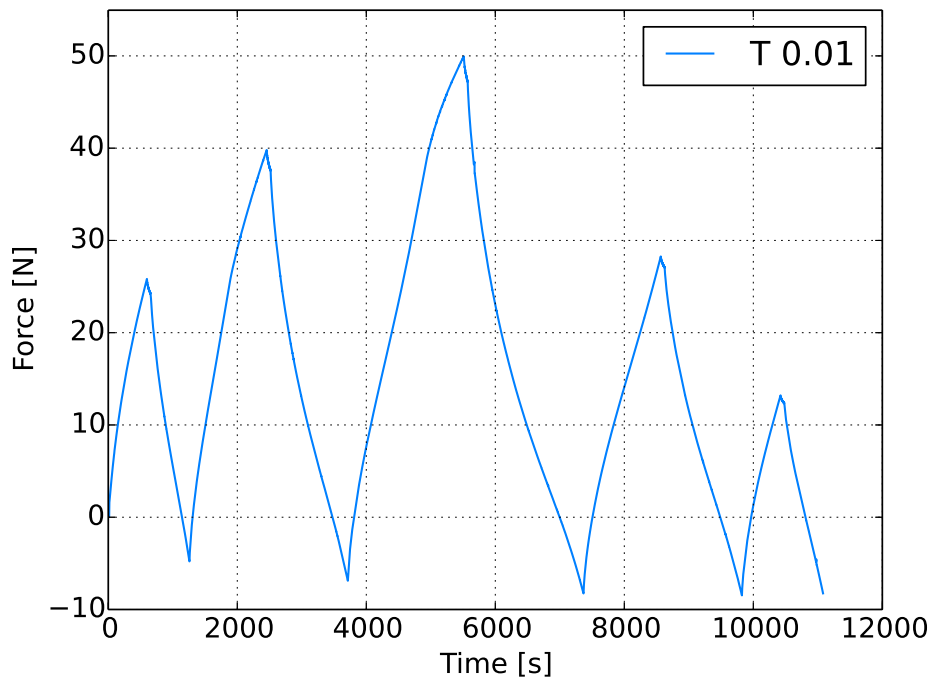


Figure 3.8: Force-time diagram: simple tension sample, strain rate 0.01 s^{-1} .

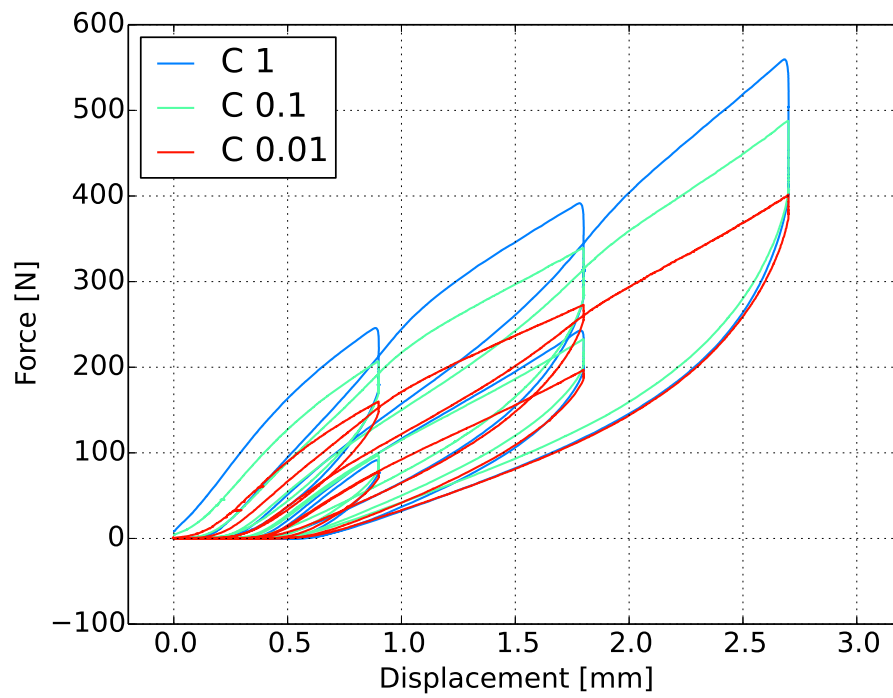
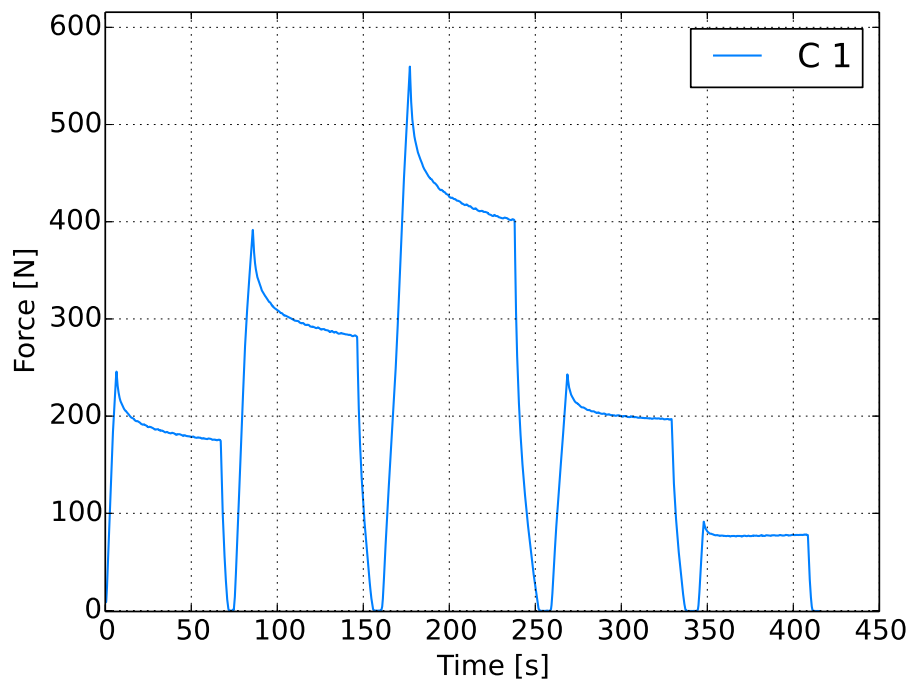


Figure 3.9: Force-Displacement diagram: simple compression samples

Figure 3.10: Force-time diagram: simple compression sample, strain rate 1 s^{-1} .

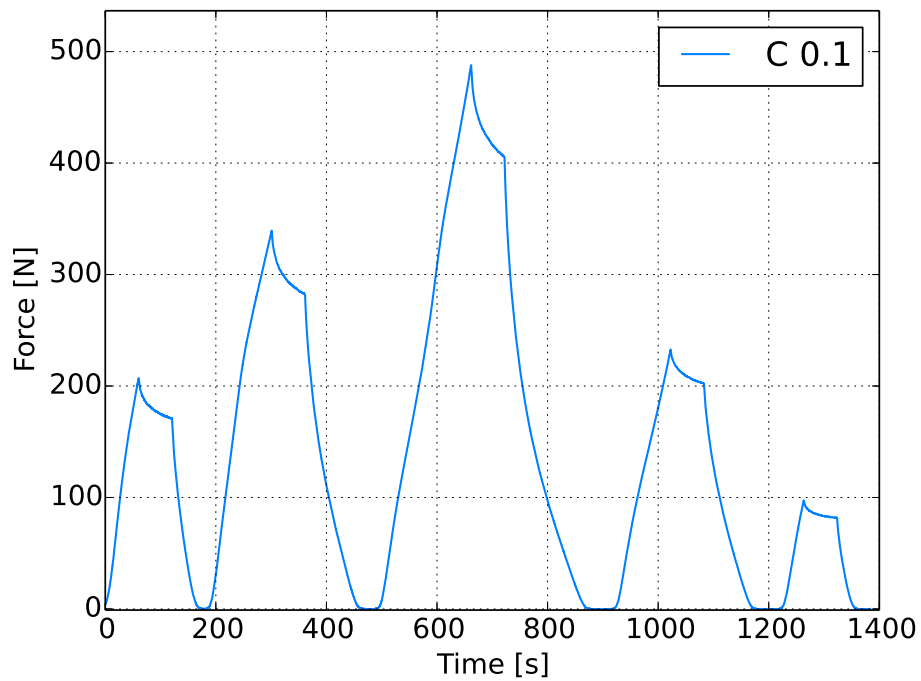


Figure 3.11: Force-time diagram: simple compression sample, strain rate 0.1 s^{-1} .

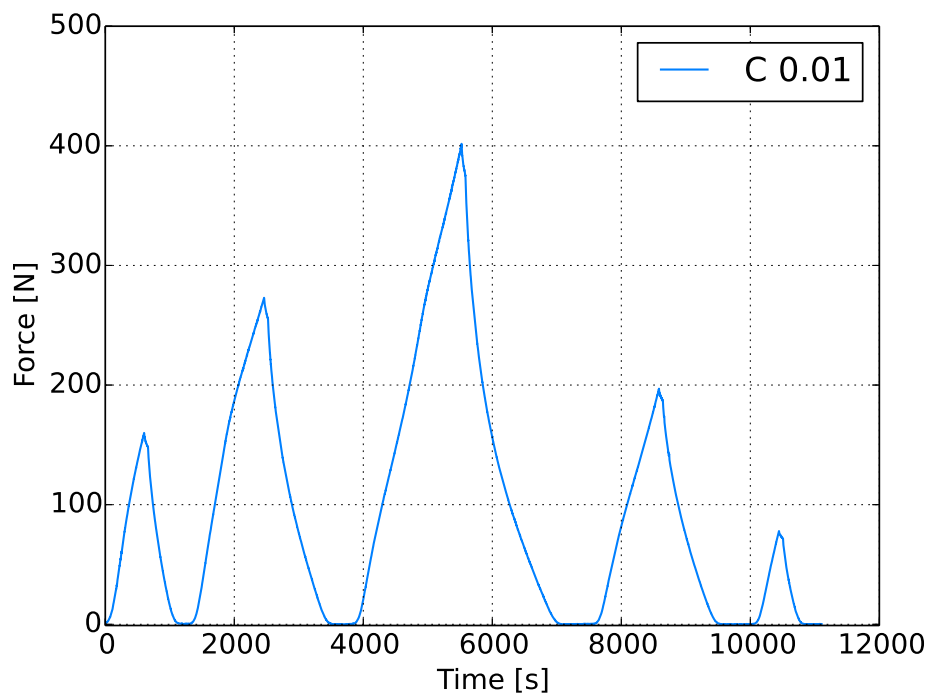


Figure 3.12: Force-time diagram: simple compression sample, strain rate 0.01 s^{-1} .

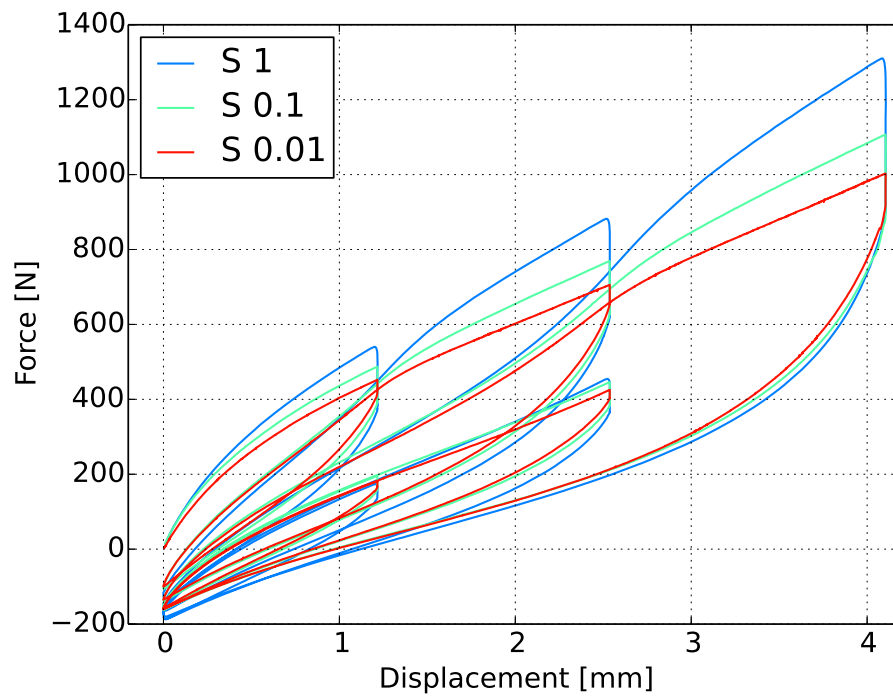
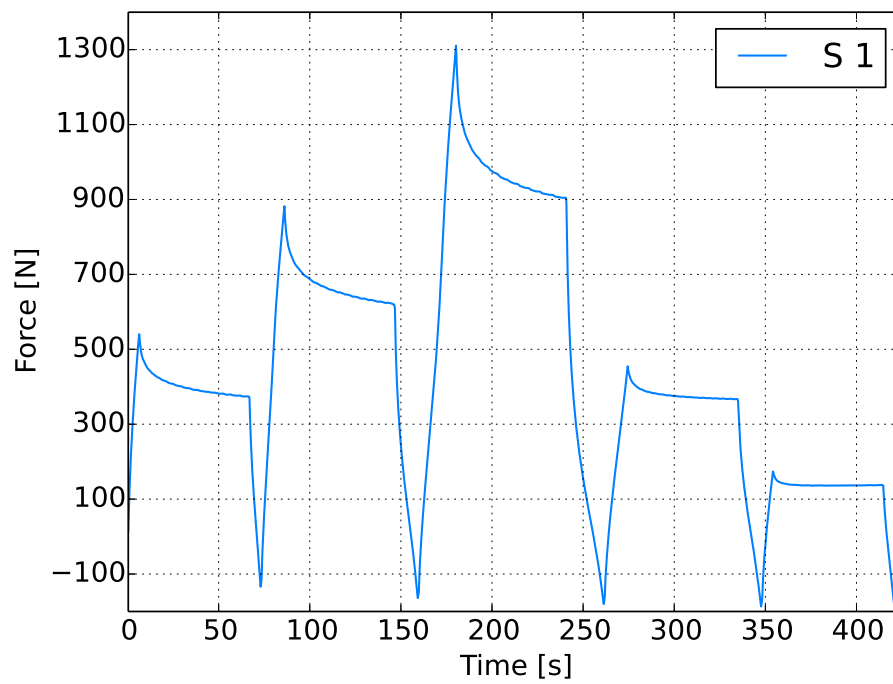


Figure 3.13: Force-Displacement diagram: shear samples

Figure 3.14: Force-time diagram: shear sample, strain rate 1 s^{-1} .

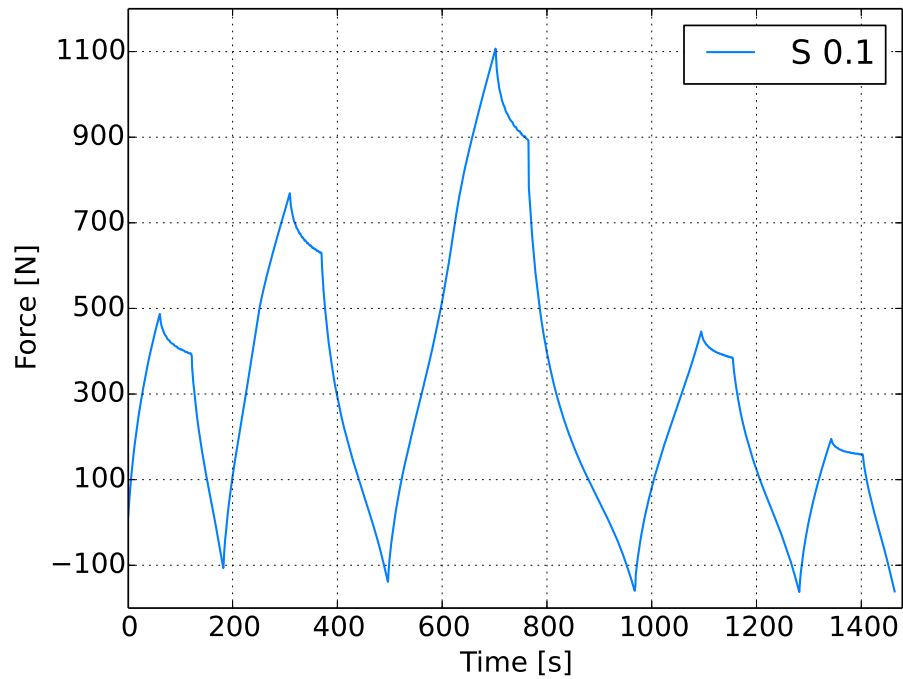


Figure 3.15: Force-time diagram: shear sample, strain rate 0.1 s^{-1} .

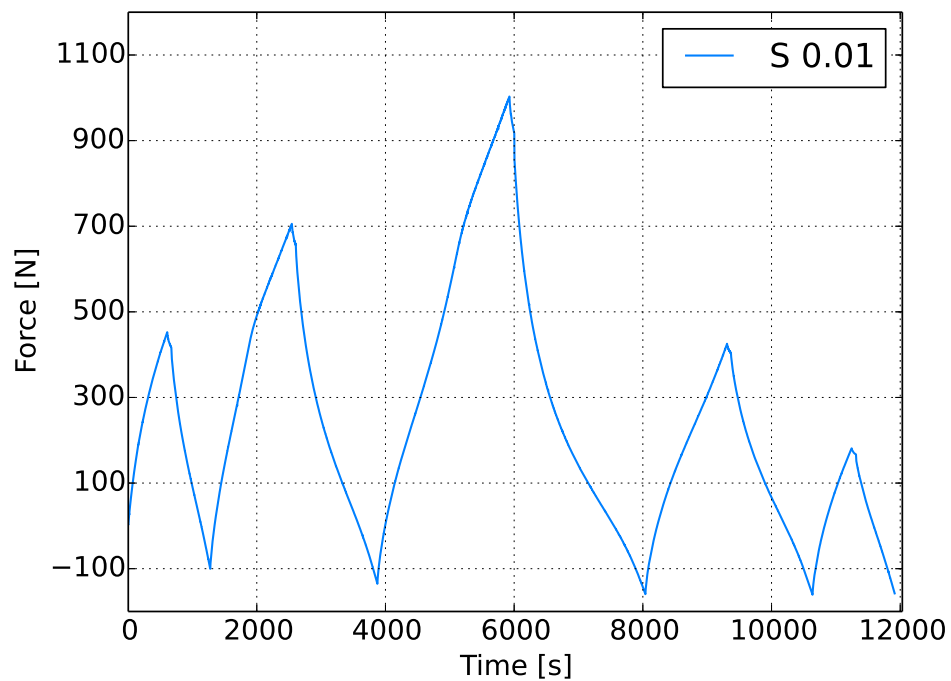


Figure 3.16: Force-time diagram: shear sample, strain rate 0.01 s^{-1} .

4 Material models

This chapter deals with isotropic material models, used for modelling of rubber-like materials. Hyperelastic, viscoelastic models and strain softening effect will be mentioned. In the second part of the chapter, one of the most advanced material models for rubber-like materials modelling, the Parallel network, will be introduced. Following models are listed in a form without temperature dependence. Due to the behaviour of rubber-like materials: large displacements, large strains and non-linear stress-strain relation, the large strain theory must be used to achieve proper results.

4.1 Elasticity

One of the basic material models is the elastic solid. Deformations of elastic solid are fully reversible, loading and unloading paths are identical as shown in Figure 4.1 (a) and (b). Stress-strain response is independent on the rate of loading or loading history. The linear elasticity theory allows us to express stress-strain relations of deformable solids for nominal strains smaller than 1%. This theory is applicable to materials with linear stress-strain relation, for example metals. For rubber-like materials, this approach is inappropriate. As an extension to rubber-like materials, hyperelastic models were invented. Using the linear elasticity, the stress strain relation can be expressed as [9]:

$$\sigma_{ij} = 2\mu\varepsilon_{ij} + \lambda\varepsilon_{kk}\delta_{ij}, \quad i, j = 1, 2, 3, \quad (4.1)$$

where σ is the engineering stress, ε is the engineering strain, μ is the shear modulus, λ is Lamé's constant and δ is the Kronecker delta function. The material is assumed to be isotropic, defined by λ and μ .

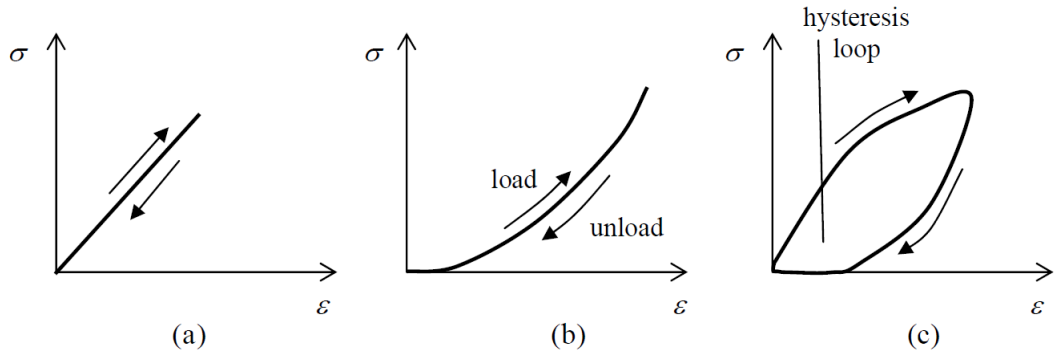


Figure 4.1: Stress-strain relationships for: (a) linear elastic material, (b) non-linear elastic material, (c) viscoelastic material [20].

4.2 Hyperelasticity

Hyperelasticity is the generalization of the linear elasticity which allows us to predict the behaviour of rubber-like and other elastic materials in the case of large strains. The stress-strain relations are expressed using the strain energy density $W(\mathbf{F})$, which is a function of the deformation gradient \mathbf{F} . It is also possible to express the strain energy density in terms of the right Cauchy-Green deformation tensor \mathbf{C} or its invariants or principal stretches.

4.2.1 Constitutive equations

The basic constitutive equation can be derived from the rate of change of strain energy density $W(\mathbf{F})$, which is given by the stress power. The stress power can be expressed using energetically conjugate stress and strain rate tensors in form [20]:

$$\dot{W} = J\boldsymbol{\sigma} : \mathbf{d} = \mathbf{P} : \dot{\mathbf{F}} = \mathbf{S} : \dot{\mathbf{E}} = \mathbf{S} : \frac{\dot{\mathbf{C}}}{2}. \quad (4.2)$$

Another possibility to express the rate of change of \dot{W} is:

$$\dot{W} = \frac{\partial W}{\partial \mathbf{F}} : \dot{\mathbf{F}}. \quad (4.3)$$

Comparing equations 4.2 and 4.3 leads to:

$$\mathbf{P} : \dot{\mathbf{F}} = \frac{\partial W}{\partial \mathbf{F}} \dot{\mathbf{F}}, \quad (4.4)$$

where $\dot{\mathbf{F}}$ can take any value. The constitutive equation for the first Piola Kirchoff stress tensor then has a form:

$$\mathbf{P} = \frac{\partial W(\mathbf{F})}{\partial \mathbf{F}}. \quad (4.5)$$

Using the same principles as above is it possible to derive alternative forms of 4.5:

$$\mathbf{S} = \mathbf{F}^{-1} \frac{\partial W(\mathbf{F})}{\partial \mathbf{F}}, \quad (4.6)$$

$$\boldsymbol{\sigma} = J^{-1} \mathbf{F} \left(\frac{\partial W(\mathbf{F})}{\partial \mathbf{F}} \right)^T. \quad (4.7)$$

When W is a function of the deformation tensors, the constitutive equations take a form:

$$\mathbf{P} = 2\mathbf{F} \frac{\partial W(\mathbf{C})}{\partial \mathbf{C}}, \quad (4.8)$$

$$\mathbf{S} = \frac{\partial W(\mathbf{E})}{\partial \mathbf{E}} = 2, \frac{\partial W(\mathbf{C})}{\partial \mathbf{C}}, \quad (4.9)$$

$$\boldsymbol{\sigma} = J^{-1} \frac{\partial W(\mathbf{E})}{\partial \mathbf{E}} \mathbf{F}^T. \quad (4.10)$$

Hyperelastic material models use the strain energy density as a function of principal invariants or principal stretches of \mathbf{C} . According to Itskov [19], the strain density function can be expressed in terms of principal invariants or principal stretches of right Cauchy-Green deformation tensor as:

$$W(\mathbf{C}) = W(I_1, I_2, I_3) = W(\lambda_1, \lambda_2, \lambda_3). \quad (4.11)$$

Principal invariants of \mathbf{C} are the following:

$$I_1 = \text{tr}(\mathbf{C}) = \lambda_1 + \lambda_2 + \lambda_3, \quad (4.12)$$

$$I_2 = \frac{1}{2} \left[(\text{tr} \mathbf{C}^2) - \text{tr}(\mathbf{C}^2) \right] = \lambda_1 \lambda_2 + \lambda_2 \lambda_3 + \lambda_3 \lambda_1, \quad (4.13)$$

$$I_3 = \det(\mathbf{C}) = \lambda_1 \lambda_2 \lambda_3. \quad (4.14)$$

Principal stretches $\lambda_i = \sqrt{\Lambda_i}$, where Λ_i ($i = 1, 2, 3$) are eigenvalues of \mathbf{C} . Substituting (4.11) into (4.9) and using the chain rule for derivatives we get constitutive equations in terms of principal invariant [23], [16]:

$$\mathbf{S} = 2 \frac{\partial W(I_1(\mathbf{C}), I_2(\mathbf{C}), I_3(\mathbf{C}))}{\partial \mathbf{C}} = 2 \sum_{i=1}^3 \frac{\partial W}{\partial I_i} \frac{\partial I_i}{\partial \mathbf{C}}, \quad (4.15)$$

or principal stretches:

$$\mathbf{S} = 2 \frac{\partial W(\lambda_1, \lambda_2, \lambda_3)}{\partial \mathbf{C}} = 2 \sum_{i=1}^3 \frac{\partial W}{\partial \lambda_i} \frac{\partial \lambda_i}{\partial \mathbf{C}}. \quad (4.16)$$

Partial derivatives of principal invariants with respect to \mathbf{C} are:

$$\frac{\partial I_1}{\partial \mathbf{C}} = \mathbf{I}, \quad \frac{\partial I_2}{\partial \mathbf{C}} = I_1 \mathbf{I} - \mathbf{C}, \quad \frac{\partial I_3}{\partial \mathbf{C}} = I_3 \mathbf{C}^{-1} \quad (4.17)$$

and partial derivatives of principal stretches with respect to \mathbf{C} are:

$$\frac{\partial \lambda_i}{\partial \mathbf{C}} = \frac{1}{2\lambda_i} \hat{N}_i \otimes \hat{N}_i, \quad (4.18)$$

where N_i is a unit vector along principle directions.

4.2.2 Decoupled Formulation

In the case of compressible hyperelastic materials, it is suitable to decompose the deformation gradient to isochoric and volumetric part [23], [20]:

$$\mathbf{F} = \mathbf{F}_{iso} \mathbf{F}_{vol}, \quad (4.19)$$

where

$$\mathbf{F}_{vol} = J^{\frac{1}{3}} \mathbf{I}, \quad (4.20)$$

$$\mathbf{F}_{iso} = J^{-\frac{1}{3}} \mathbf{F}. \quad (4.21)$$

The isochoric parts of tensors, invariants and stretches ($\bar{A} = \bar{A}_{iso}$) can be determined as:

$$\bar{\mathbf{C}} = \bar{\mathbf{F}}^T \bar{\mathbf{F}} = J^{-\frac{2}{3}} \mathbf{C}, \quad (4.22)$$

$$\bar{I}_1 = J^{-\frac{2}{3}} I_1, \quad \bar{I}_2 = J^{-\frac{4}{3}} I_2, \quad \bar{I}_3 = 1, \quad (4.23)$$

$$\bar{\lambda}_i = J^{-\frac{1}{3}} \lambda_i. \quad (4.24)$$

The strain energy density can be decoupled to volumetric and isochoric part in a similar way as the deformation gradient:

$$W = W_{vol}(J) + W_{iso}(\bar{\mathbf{C}}). \quad (4.25)$$

Hyperelastic material models use this decomposition to define total strain energy density, as will be shown in the next part. Using (4.9) and the decoupled formulation of W (4.25), constitutive equation can be expressed as:

$$\mathbf{S} = 2 \underbrace{\frac{\partial W}{\partial \mathbf{C}}}_{\mathbf{S}} = 2 \underbrace{\frac{\partial W_{vol}}{\partial \mathbf{C}}}_{\mathbf{S}_{vol}} + 2 \underbrace{\frac{\partial W_{iso}}{\partial \mathbf{C}}}_{\mathbf{S}_{iso}}. \quad (4.26)$$

4.2.3 Hyperelastic material models

Hyperelastic material models define the strain energy density. It is possible to divide these models into phenomenological and mechanistic. Phenomenological models try

to describe observed behaviour without any physical meaning. Mechanistic models are based on material structure. Models which combine both approaches are called hybrid. Following material models are given for compressible isotropic materials, where volumetric parts of strain energy density are defined using the volume ratio J . Overlined tensors and invariants are called modified and denote isochoric parts of quantities as shown in equations (4.22), (4.23) and (4.24). Given terms are taken over from [1] and as a source of information, [6], [2] and [23] were used.

Neo-Hookean model

Neo-Hookean is one of the simplest hyperelastic models. Strain density function is defined using first invariant as:

$$W = C_1(\overline{I}_1 - 3) + \frac{1}{D_1}(J - 1)^2, \quad (4.27)$$

where J is the volume ratio, C_1 [Nm^{-2}] and D_1 [N^{-1}m^2] are material parameters, which can be obtained from relations:

$$C_1 = \frac{\mu}{2}, \quad D_1 = \frac{2}{K}.$$

Parameter μ is the shear modulus and K is the bulk modulus. Neo-Hookean model belongs to mechanistic models and assumes that μ can be obtained using statistical mechanic in form:

$$\mu = NkT, \quad (4.28)$$

where N is a number of polymer chains per unit volume, k is the Boltzmann constant and T is temperature.

Generalized polynomial model

Generalized polynomial model is phenomenological model which defines the strain energy density using first and second invariants:

$$W = \sum_{i+j=1}^N C_{ij}(\overline{I}_1 - 3)^i(\overline{I}_2 - 3)^j + \sum_{m=1}^M \frac{1}{D_m}(J - 1)^{2m}, \quad i, j \in \mathbb{N}. \quad (4.29)$$

Material parameters are C_{ij} [Nm^{-2}] and D_i [N^{-1}m^2]. For small strains, the parameters C_{10} , C_{01} and D_1 must correspond with the initial shear modulus μ_0 and the initial bulk modulus K_0 :

$$\mu_0 = 2(C_{10} + C_{01}) \text{ and } K_0 = \frac{2}{D_1}.$$

For parameters $N = 1$ and $M = 1$ we obtain Mooney-Rivlin model, which is quite often used to model behaviour of rubber-like materials.

Reduced polynomial model

This model is similar to the previous case, but it uses just the first invariant to define the strain energy density in the following form:

$$W = \sum_{i=1}^N C_{i0} (\bar{I}_1 - 3)^i + \sum_{n=1}^N \frac{1}{D_n} (J - 1)^{2i} \quad (4.30)$$

Initial shear modulus and initial bulk modulus correspond with:

$$\mu_0 = 2C_{10} \text{ and } K_0 = \frac{2}{D_1}.$$

Ogden model

One of the most precise phenomenological material models for rubber-like material modelling is Ogden model, which defines the strain energy density as a function of principal stretches:

$$W = \sum_{i=1}^N \frac{2\mu_i}{\alpha_i^2} (\bar{\lambda}_1^{\alpha_i} + \bar{\lambda}_2^{\alpha_i} + \bar{\lambda}_3^{\alpha_i} - 3) + \sum_{j=1}^3 \frac{1}{D_j} (J - 1)^{2j}. \quad (4.31)$$

Material parameters are α_i [-], μ_i [Nm⁻²] and D_j [N⁻¹m²]. For small strains the initial shear modulus must correspond with:

$$\mu_0 = \sum_{i=1}^N \mu_i. \quad (4.32)$$

Arruda-Boyce model

This mechanistic hyperelastic model is based on eight-chain representation of underlying structure of rubber and non-Gaussian behaviour of chains [6]. Strain density can be defined as:

$$W = \mu \sum_{i=1}^5 \frac{C_i}{\lambda_n^{2i-2}} (\bar{I}_1^i - 3^i) + \frac{1}{D} \left(\frac{J^2 - 1}{2} - \ln(J) \right). \quad (4.33)$$

where C_i is the first five members of Taylor's expansion of inverse Langevin function. Langevin function is defined as:

$$L(x) = \coth(x) - \frac{1}{x}. \quad (4.34)$$

Material parameters are μ [Nm⁻²], λ_m [-] and D [N⁻¹m²]. λ is a parameter of locking-stretch which defines the value of chain stretch when the chain length reaches fully

extended state [6]. Parameters μ and $D = \frac{1}{K}$ correspond to the initial shear modulus and the initial bulk modulus for small strains. The representation of 8 chain model is showed in figure 4.2.

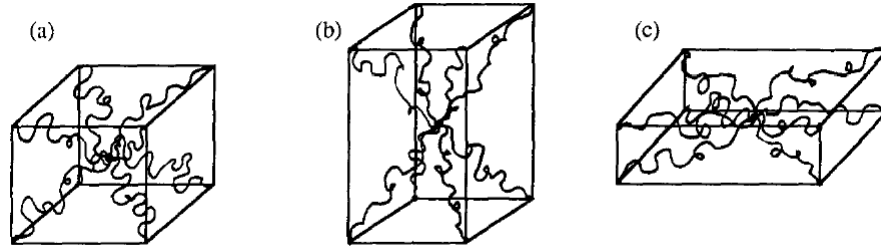


Figure 4.2: Representation of 8 chain model in (a) undeformed, (b) uniaxial extension and (c) biaxial extension configurations [6].

4.3 Strain softening

Strain softening effect can be observed during the cyclic loading of rubber like materials. This effect was intensively investigated by Mullins and his co-workers and therefore the stress softening effect is also known as Mullins effect. The strain softening can be considered as a damage accumulation in the material [9], [12].

The typical behaviour of rubber-like materials that exhibit Mullins effect [9]: The stress at given strain is the highest in the first loading cycle. The amount of damage is also highest in the first loading cycle and decreases with further cycles. After few cycles the material response for given strain becomes identical and the material is preconditioned. The amount of damage is dependent on maximal applied strain. Damage caused by Mullins effect is not permanent, there is a recovery going on over time.

The mechanism of damage caused by strain softening is still not fully discovered. In [12] is summarised information about Mullins effect and its mechanism. In most of the finite element based software, Ogden-Roxborough model is available for Mullins effect. This model is described in section 4.5.3. Another model for Mullins effect is Qi-Boyce model [7], but this model is not yet implemented in finite element based software products.

4.4 Viscoelasticity

Viscoelastic solid is a combination of elastic solid and viscous fluid. Deformations of viscoelastic solid are not fully reversible, loading and unloading paths are not identical and they form a hysteresis loop. In comparison to elastic solids, viscoelastic solids are strain rate dependent. Both mentioned behaviours are shown in Figure 4.3. Strain rate dependence implies that the viscoelastic material response depends on time. Actual behaviour of material during a load depends on previous history of loading.

Viscoelastic models are represented by elastic springs and viscous dashpots. In Figure 4.4, the basic viscoelastic models are shown. Details of the basic viscoelastic model can be found in [17]. In this thesis only the Prony series will be mentioned, which is the most common way to model large strain viscoelasticity using finite element based computation software.

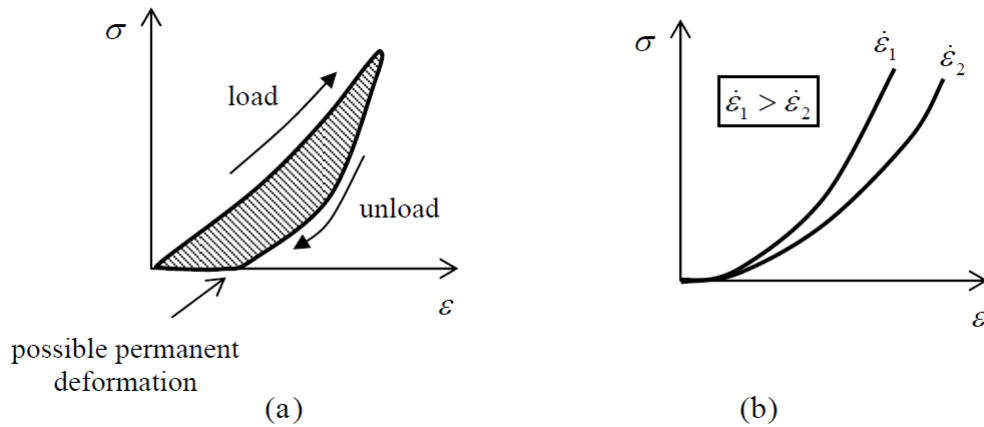


Figure 4.3: Response of viscoelastic material: (a) loading a unloading, (b) different strain rate stretching [21]

4.4.1 Small strain linear viscoelasticity

Small strain linear viscoelastic material model is based on linear elasticity and linear viscoelasticity. Constitutive equation in 1D is given by Boltzmann integral [9]:

$$\sigma(t) = \int_{-\infty}^t E_R(t - \tau) d\varepsilon(t) = \int_{-\infty}^t E_R(t - \tau) \frac{d\varepsilon}{d\tau} d\tau, \quad (4.35)$$

where E_R is the relaxation modulus and τ is the integration variable. Small strain viscoelasticity is not accurate enough to predict behaviour of rubber-like materials.

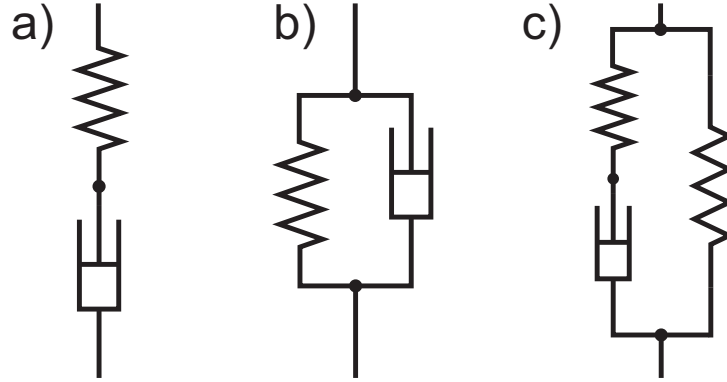


Figure 4.4: Schemes of viscoelastic models (a) Maxwell model, (b) Voigt model and (c) standard linear solid model

4.4.2 Large strain linear viscoelasticity

This theory is used to predict behaviour of rubber-like materials. It is a combination of hyperelasticity and linear viscoelasticity. Constitutive equation in 1D can be derived from equation 4.35 [9]:

$$\sigma(t) = \int_{-\infty}^t E_R(t - \tau) d\varepsilon(t) = \int_{-\infty}^t E_R(t - \tau) \frac{d\varepsilon}{d\tau} d\tau. \quad (4.36)$$

By integrating this equations in part we obtain:

$$\sigma(t) = E_0 \varepsilon(t) - \int_0^t \dot{q}_R(t - \tau) E_0 \varepsilon(\tau) d\tau, \quad (4.37)$$

where $g_R(t) = \frac{E_R(t)}{E_0}$ is the normalized relaxation modulus, E_0 is the instantaneous Young's modulus. Hyperelastic stress function can be defined as:

$$\sigma_{hyp}(\varepsilon) = \sigma_{hyp}(\varepsilon(t)) = E_0 \varepsilon(t). \quad (4.38)$$

Substituting (4.38) into (4.37) we obtain constitutive equation:

$$\sigma(t) = \sigma_{hyp}(\varepsilon(t)) - \int_0^t \dot{q}_R(t - \tau) \sigma_{hyp}(\varepsilon(\tau)) d\tau \quad (4.39)$$

which shows the combination of stress relaxation function and hyperelastic stress function. The most common way to represent normalised relaxation modulus g_R or relaxation modulus E_R is the Prony series. Hyperelastic stress function was generally defined in the previous part.

4.4.3 Prony series

The Prony series defines the normalised relaxation modulus g_R in form of series expansion:

$$g_R(t) = \frac{E_R(t)}{E_0} = 1 - \sum_{i=1}^N g_i \left(1 - e^{-\frac{t}{\tau_i}}\right), \quad (4.40)$$

where τ_i is the relaxation time and g_i is normalised relaxation modulus of i th network. Prony series can be formulated in term of relaxation modulus $E_R(t)$, this formulation is equivalent to multi-network Maxwell model [9] and relaxation modulus has a form [27]:

$$E_R(t) = E_\infty + \sum_{i=1}^n E_i e^{-\frac{t}{\tau_i}}, \quad (4.41)$$

where E_i is the relaxation modulus and τ_i is the relaxation time of i th network. E_∞ is the long term modulus, which represents totally relaxed state of material. Scheme of Prony series is showed in Figure: 4.5.

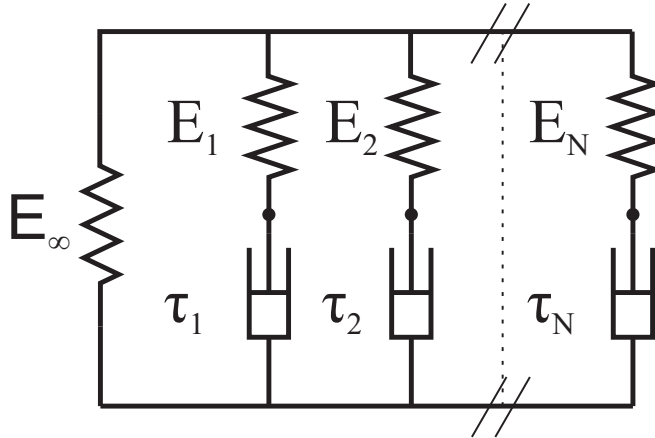


Figure 4.5: Schemes of the Prony series

4.5 Parallel network model

This section deals with the Parallel network (PN) model which is suitable for describing non-linear viscoelastic behaviour of rubber-like materials. PN model allows to combine several material models in one framework. Non-linear viscoelasticity, plasticity, Mullins effect, permanent set and many other models are available in this framework. PN model used in this thesis was reduced to non-linear viscoelasticity with combination of Mullins effect. Plasticity was not used in this case. Information about this model comes mainly from [18] and [11], [1].

Parallel network model can be represented by scheme in Figure 4.6, where network 0 is called the equilibrium network and consists of an elastic and a plastic element. Networks 1, 2, 3... N are viscoelastic networks. For each network, multiplicative split of the deformation gradient \mathbf{F} is assumed:

$$\mathbf{F} = \mathbf{F}_0^e \mathbf{F}_0^{pl}, \quad i = 0 \quad (4.42)$$

$$\mathbf{F} = \mathbf{F}_i^e \mathbf{F}_i^{cr}, \quad i = 1, 2, \dots, N, \quad (4.43)$$

where \mathbf{F}^e is elastic part of the deformation gradient, \mathbf{F}^{pl} is the creep part of the deformation gradient in the viscoelastic networks. \mathbf{F}^{cr} is the plastic component in the equilibrium network. Response of material is assumed to be isotropic, plasticity and creep flow are assumed to be incompressible.

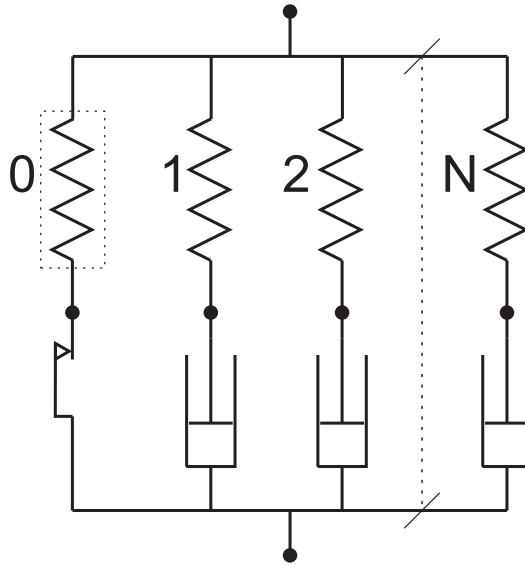


Figure 4.6: Scheme of PNM

4.5.1 Elastic response

Elastic response for i th network can be determined using hyperelastic strain energy density function in the form

$$W_i = W_i(\mathbf{C}_i^e), \quad i = 0, 1, 2, \dots, N, \quad (4.44)$$

where \mathbf{C}_i^e is the elastic right Cauchy-Green tensor for each network. All of the networks have the same definition of strain energy density function. Total strain energy W_T is equal to the weighted sum of strain energies of all the networks:

$$W_T = \sum_{i=0}^n s_i W(\mathbf{C}_i^e), \quad (4.45)$$

where s_i represents the stiffness ratio of the particular network. s_i expresses the volume fraction of i th network and sum of stiffness ratios must satisfy the following relation:

$$\sum_{i=0}^n s_i = 1. \quad (4.46)$$

Total stress response can be expressed as:

$$\boldsymbol{\tau} = \sum_{i=0}^N s_i \left\{ \mathbf{F}_i^e 2 \frac{\partial W(\mathbf{C}_i^e)}{\partial \mathbf{C}_i^e} (\mathbf{F}_i^e)^T \right\} = \sum_{i=0}^N s_i \boldsymbol{\tau}_i, \quad (4.47)$$

where $\boldsymbol{\tau}_i$ is Kirchhoff stress in i th network and $\boldsymbol{\tau} = J\boldsymbol{\sigma}$ is total Kirchhoff stress, $\boldsymbol{\sigma}$ is Cauchy stress and $J = \det(\mathbf{F})$ is the volume ratio.

4.5.2 Viscous response

Using the multiplicative split of the deformation gradient into elastic and creep, the rate form of the creep deformation gradient for each viscoelastic network ($i = 1, 2, \dots, N$) can be expressed as [18]:

$$\dot{\mathbf{F}}^{cr} = (\mathbf{F}^e)^{-1} \cdot \mathbf{D}^{cr} \cdot \mathbf{F}^e \cdot \mathbf{F}^{cr}, \quad (4.48)$$

where \mathbf{D}^{cr} is the creep part of the deformation rate tensor in the current configuration. We assume that \mathbf{D}^{cr} can be derived using a creep potential $G^{cr} = G^{cr}(\boldsymbol{\tau})$ and the flow rule in form:

$$\mathbf{D}^{cr} = \dot{\lambda} \frac{\partial G^{cr}(\boldsymbol{\tau})}{\partial \boldsymbol{\tau}}, \quad (4.49)$$

where $\dot{\lambda}$ is the proportionality factor in form $\dot{\lambda} = \dot{\bar{\epsilon}}^{cr}$ and $G^{cr}(\boldsymbol{\tau}) = q$ is effective Kirchhoff stress. Substituting previous relations into equation 4.49, the creep part of the deformation tensor \mathbf{D}^{cr} can be expressed as [18]:

$$\mathbf{D}^{cr} = \frac{3}{2q} \dot{\bar{\epsilon}}^{cr} \cdot \bar{\boldsymbol{\tau}}, \quad (4.50)$$

where $\bar{\boldsymbol{\tau}}$ is deviatoric Kirchhoff stress and $\dot{\bar{\epsilon}}^{cr}$ is the equivalent creep strain rate, which can be obtained from evolution laws. In general, $\dot{\bar{\epsilon}}^{cr}$ is a function of temperature θ , the first invariant of the creep strain tensor $I_1^{cr} = \text{tr}(\mathbf{C}^{cr})$, effective Kirchhoff stress q and the equivalent creep strain $\bar{\epsilon}^{cr}$:

$$\dot{\bar{\epsilon}}^{cr} = f(\theta, \bar{\epsilon}^{cr}, q, I_1^{cr}). \quad (4.51)$$

In Abaqus 6.14 we can find four evolution laws and there is a possibility to define own evolution law, which satisfies the equation (4.51). Evolution laws usable in PN model are listed below.

Strain hardening power law

$$\dot{\bar{\varepsilon}}^{cr} = (Aq^n [(m+1)\bar{\varepsilon}^{cr}]^m)^{\frac{1}{m+1}} \quad (4.52)$$

Parameters: $A > 0$ [$\text{N}^{-n}\text{m}^{2n}\text{s}^{(-1-m)}$], $m \in [-1, 0]$ [-] and $n > 0$ [-]. With suitable choice of parameters ($n = 1$ and $m = 0$) it is possible to create a model of a linear dashpot with viscosity $\mu = \frac{1}{A}$.

Hyperbolic-sin law model

$$\dot{\bar{\varepsilon}}^{cr} = A (\sinh(B\tilde{q}))^n \quad (4.53)$$

For HS-law, the parameters are: $A \geq 0$ [s^{-1}], $B \geq 0$ [N^{-1}m^2], $n \geq 0$ [-].

Bergstrom-Boyce model

$$\dot{\bar{\varepsilon}}^{cr} = A (\lambda^{cr} - 1 + E)^C q^m, \quad (4.54)$$

$$\lambda^{cr} = \sqrt{\frac{1}{3} \mathbf{I} : \mathbf{C}^{cr}}, \quad (4.55)$$

where parameters are $A \geq 0$ [$\text{s}^{-1}\text{N}^{-1}\text{m}^2$], $C \in [-1, 0]$ [-], $E \geq 0$ [-] and $m > 0$ [-].

Power law

Power law is available since Abaqus 6.14, which is more general form of Strain hardening power law:

$$\dot{\bar{\varepsilon}}^{cr} = \dot{\varepsilon}_0 \left(\left(\frac{q}{q_0 + \langle p \rangle} \right)^n [(m+1)\bar{\varepsilon}^{cr}]^m \right)^{\frac{1}{m+1}}, \quad (4.56)$$

where q is the Kirchhoff stress and p is the Kirchhoff pressure and parameters are: $q_0 > 0$ [Nm^{-2}], $m \in [-1, 0]$ [-], $n > 0$ [-], $a > 0$ [-] and $\dot{\varepsilon}_0 > 0$ [s^{-1}].

4.5.3 Mullins effect

Stress softening effect known as Mullins effect is included in the PN model where modified Ogden-Roxbourn model is used. Stress softening is applied to equilibrium network, where the strain energy density is modified by a damage term and has the following form:

$$W_0 = \eta W(\mathbf{C}_0^e) + \phi(\eta), \quad (4.57)$$

where η is the scalar damage variable and $\phi(\eta)$ is the smooth damage function. The spring inside the dashed box in Figure 4.3 represents the damaged elastic element. The evolution equation of the damage variable for Ogden-Roxbourn [28] model is following:

$$\eta = 1 - \frac{1}{r} \operatorname{erf} \left(\frac{\overline{W}_0^{\max} - \overline{W}_0^{\text{primary}}}{m + \beta \overline{W}_0^{\max}} \right) \quad (4.58)$$

W_0^{primary} is the deviatoric part of the strain energy in the primary loading path, W_0^{\max} is the maximum of W_0^{primary} at material point. Material parameters are $r \geq 1[-]$, $m \geq 0 [J]$, $\beta \geq 0 [-]$.

4.5.4 PN model in Abaqus

The Parallel network model consists of several networks with several material models. Each of the material models must be specified separately. PN model uses just one definition of hyperelastic elements common for all of the networks. Mullins effect is applied only onto the elastic element in the equilibrium network. Plastic element occurs only once, in the equilibrium network. Previously mentioned material models can be set using Abaqus CAE or python script. However, the definition of viscoelastic networks can't be done using Abaqus CAE or python script, so the input file of a model must be modified. For the material model used in this thesis, the material definition section in the input file has the following form:

```
** MATERIALS
**
*Material , name=Corkrubber
*Hyperelastic , arruda-boyce
500000., 1.01, 1e-05
*Mullins Effect
3., 0.50001, 0.10001
*VISCOELASTIC, NONLINEAR, NETWORKID=1, SRATIO=0.100, LAW=STRAIN
1e-15, 1.00001, 1.00001
*VISCOELASTIC, NONLINEAR, NETWORKID=2, SRATIO=0.100, LAW=STRAIN
1e-15, 1.00001, 1.00001
*VISCOELASTIC, NONLINEAR, NETWORKID=3, SRATIO=0.100, LAW=STRAIN
1e-15, 1.00001, 1.00001
**.
```

Each of the viscoelastic networks must be defined by network id number, definition of the stiffness ratio, the evolution law and material parameters as shown above. Sum of the stiffness ratios must satisfy the equation 4.46. Stiffness ratio of equilibrium network is defined as:

$$s_0 = 1 - \sum_{i=1}^N s_i, \quad (4.59)$$

where i is id number of viscoelastic network and N is the total number of networks. Particular viscous law can be specified in the input file using commands given in Table 4.1 and appropriate material parameters. A detailed description of material parameters can be found in [1].

Table 4.1: Viscous evolution law definition

Law	Command	Parameters
Strain hardening power law	LAW=STRAIN	A, n, m
Hyperbolic-sin law model	LAW=HYPERB	A, B, n
Bergstrom-Boyce model	LAW=BERGSTROM-BOYCE	A, m, C, E
Power law	LAW=POWER LAW	$q_0, n, m, a, \dot{\epsilon}$

5 Material parameters calibration

Previous chapters were a preparation for a material parameters calibration, which is based on comparison of results of experiments and results of numerical simulations. This approach is called curve fitting. For proper material parameters, the difference between the experiments and simulations is minimal. The process of searching for proper material parameters is called material parameter calibration. In this scenario, material parameters will be searched using optimisation methods.

In the following section numerical simulations, chosen material model, principles of numerical optimisations, definition of the objective function and the optimisation task will be introduced. Last section of this chapter will be aimed at processing of the cork-rubber composite material parameters calibration.

5.1 Numerical simulations

For the purpose of material parameters calibration, numerical simulations based on finite element method were created. Numerical simulations of uniaxial tension, uniaxial compression and simple shear were created in Abaqus 6.14. All finite element models were created using Python scripts, which allows us to change their properties parametrically. For every single numerical simulation, a finite element model is built, with given properties.

Finite element models were created to correspond with the performed experiments. Due to material parameters, calibration must be as simple as possible to save computational time. Each sample is symmetric in some way, and so this property is used for creating the finite models.

5.1.1 Uniaxial tension

Samples used in the uniaxial experiments have the shape of a dog bone. The displacement was measured by mechanical extensometer in the central part of the samples, which is shown in Figure 3.2 (a). To make the finite element model more simple, only the central parts of the samples were created. In addition, the symmetry of this part was used and just 1/8 of the central part of the dog bone forms the finite element model shown in Figure 5.1. These simplifications allow us to define boundary conditions more easily and make the numerical simulations less time consuming.

Two types of boundary conditions were defined. Due to the symmetry of the central part, symmetry boundary conditions defined on surfaces showed in Figure 5.1 were used. Symmetry boundary conditions disable displacements in the directions perpendicular to a chosen plane. Results of numerical simulations, where the symmetry BC was used, must be recalculated in order to get valid values. In this case the total reaction force in bottom surface must be multiplied by 4 and displacement of the top surface must be multiplied by 2. The displacement boundary condition in y direction given by loading history was set on the top surface of the part as shown in Figure 5.1.

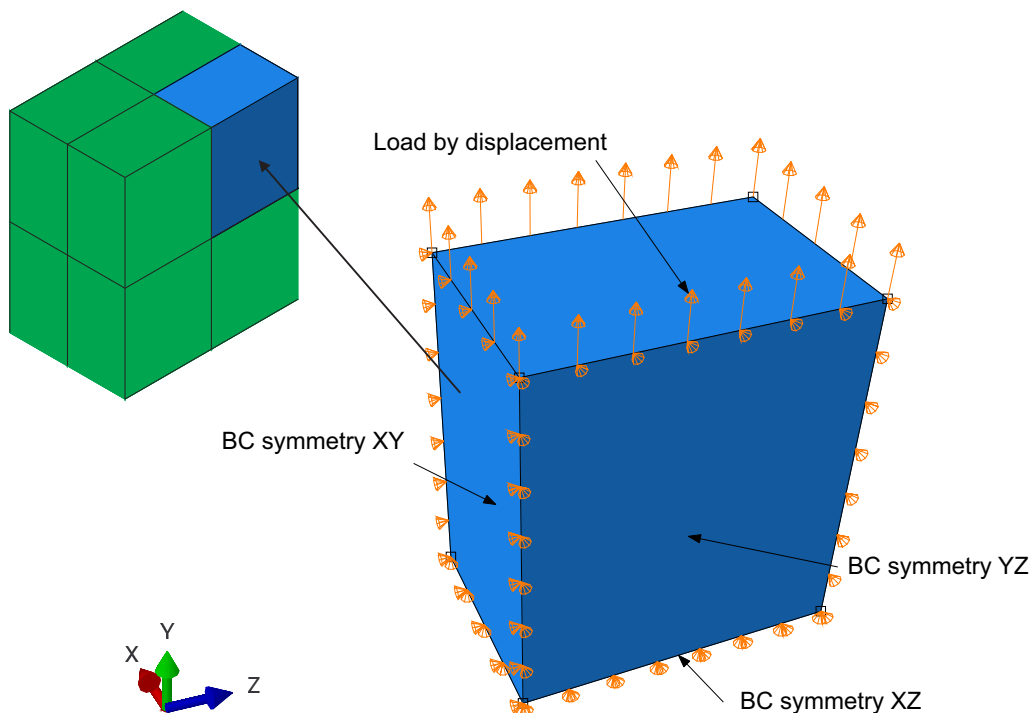


Figure 5.1: Boundary conditions of tension model

Finite element mesh of uniaxial tension model consists of only one linear brick element with hybrid formulation. Due to uniform stress and strain distribution, one single element is accurate enough. There is no significant change in results for a finer mesh.

5.1.2 Uniaxial compression

Finite element model of uniaxial compression consists of the compression sample and 2 rigid parts, which represent clamps of the testing machine. The compression sample is rotationally symmetrical, which allows us to reduce this 3D model to more simple 2D model. The finite element model is formed by one half of the cross-section of the sample as shown in Figure: 5.2. Numerical simulation of uniaxial compression is more complicated than the previous one, because of an interaction between the rigid parts and the cork-rubber sample. This interaction was set using a general contact, where the friction coefficient between rigid parts and cork-rubber composite was set to 0.6. Friction parameter of cork-rubber composite is not known, the only available information is about cork-steel friction parameter, which is equal to 0.63 [29].

Boundary conditions were set to rigid parts as shown in Figure 5.2, where the bottom part was fixed in all directions and the displacement of the top rigid part in y direction was given by the loading history. The finite element mesh of uniaxial compression model was created using axisymmetric linear elements with hybrid formulation. Numerical simulations of uniaxial compression did not converge well. Due to large strains and high friction coefficient, the elements distortion appeared and simulations failed. In order to find the ideal size of the mesh, two types of meshes were investigated, however no universal size or type of mesh which ensures higher stability of simulations was found. The investigated finite element meshes are shown in Figure 5.2, where the size of (a) elements is 1 mm. The size of (b) elements is from 1 mm to 0.2 mm.

The finite element mesh (a) is not so accurate, but it showed that large elements are better in case of contact simulation of uniaxial compression. Using mesh (b) with smaller elements we obtain more accurate solution, but it costs more computational time and small elements caused higher convergence errors than larger elements. In section 5.5 are described problems with convergence of uniaxial compression simulations. Stability and convergence problems of contact type simulations are topics for author's next research.

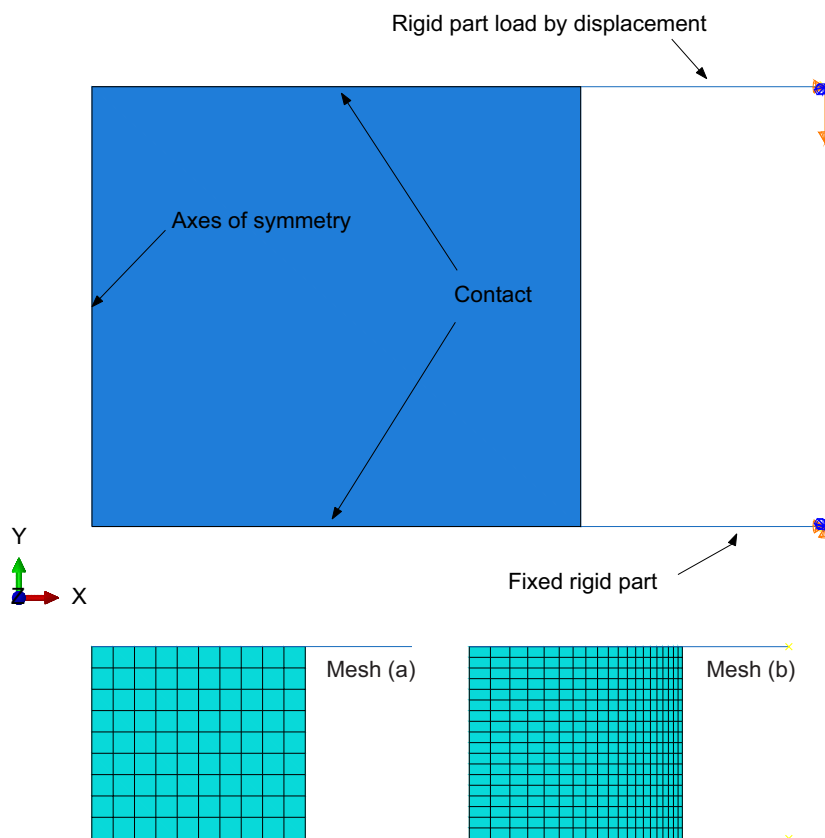


Figure 5.2: Boundary conditions and mesh of uniaxial compression finite element model

5.1.3 Simple shear

The last of the created models is the model of simple shear. Geometry of the sample allows us to use symmetry similarly to the tension model, as shown in Figure 5.3. Finite element model of simple shear only consists of the shear sample, the steel parts are not modelled. Boundary conditions are set directly on the sample.

The bottom surface of the part was fixed in all directions and the displacement of top surface in x direction is given by the loading history. The last boundary condition is the symmetry, which was set to surface shown in Figure 5.3.

Finite element mesh of simple shear model was created using linear brick elements with hybrid formulation. The finite element mesh is shown in Figure 5.3. Elements size is 2 mm.

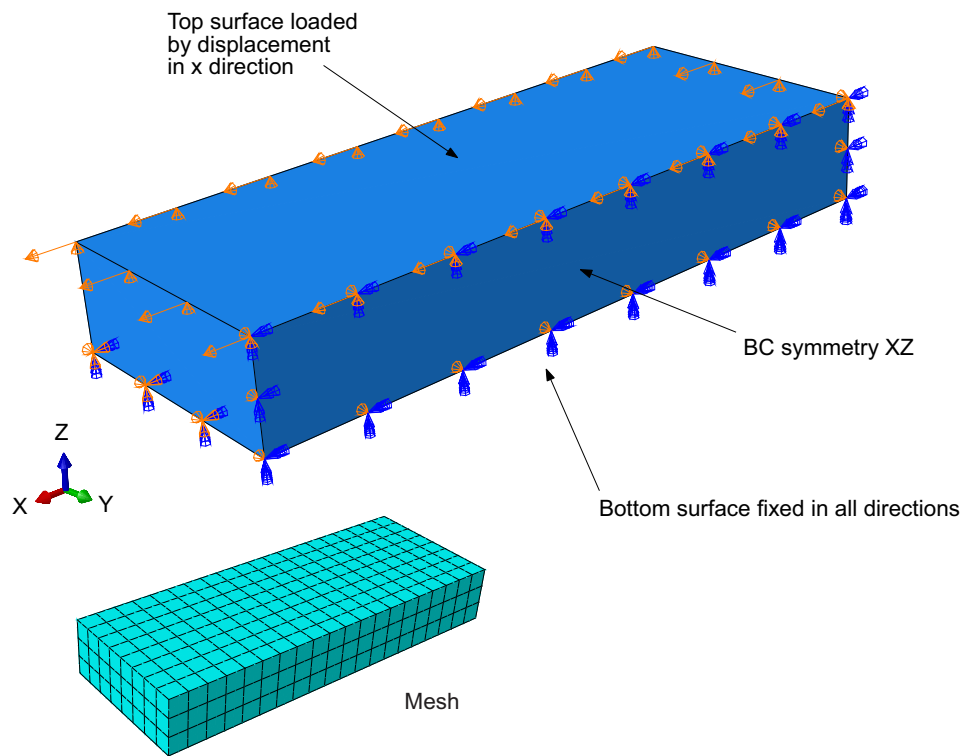


Figure 5.3: Boundary conditions and mesh of simple shear finite element model

5.1.4 Material model

Parallel network model was chosen as the material model. This model consists of hyperelastic elements defined using Arruda-Boyce model, three viscoelastic networks defined using the Strain hardening power law and Mullins effect represented by the Ogden-Roxbourg model. Used models are summarized in Table 5.1. This model contains 18 parameters which must be calibrated.

Arruda-Boyce model was chosen due to its unconditional stability, accuracy and a low number of parameters. Strain hardening power law was chosen because of the possibility to reduce non-linear viscoelastic model to linear viscoelastic model. It is less complicated to start with calibration of linear model parameters and then introduce non-linear model.

Table 5.1: Used material model

Element	Model/law	Parameters
Hyperelastic	Arruda-Boyce	μ, λ, D
Viscoelastic	Strain hardening power law	A_1, n_1, m_1, s_1
Viscoelastic	Strain hardening power law	A_2, n_2, m_2, s_2
Viscoelastic	Strain hardening power law	A_3, n_3, m_3, s_3
Strain softening	Ogden-Roxbourg	r, m, β

5.2 Numerical Optimization

Numerical optimisation is the process of minimization of a function subject to constraints on its variable, mathematically it can be written in form [26]:

$$\min_{\mathbf{x} \in \mathbb{R}^n} f(\mathbf{x}) \quad \text{subject to} \quad \begin{cases} c_i(\mathbf{x}) = 0, & i \in \varepsilon; \\ c_i(\mathbf{x}) \geq 0, & i \in \mathbb{I}; \end{cases}, \quad (5.1)$$

where \mathbf{x} is the vector of parameters, f is the objective function that will be minimized, \mathbf{c} is the vector of constraints and ε and \mathbb{I} are sets of indices.

Numerical optimisation can be divided into unconstrained and constrained. Constrained optimisation has explicitly defined constraints on the variables. These constraints may define bounds of parameters such as $0 \leq x_1 \leq 1$ or be more complex and represent the relationship between parameters, such as: $\sum_{i=1}^3 x_i = 1$. Constrained optimisation was used in material parameter calibration and both of the listed constraints were used.

Numerical optimisation was performed using Optislang 4.2 which is a software for sensitivity analysis, multiobjective and multidisciplinary optimisation. Many optimisation

algorithms are available in Optislang. For this scenario, an evolution algorithm and a gradient based algorithm were chosen.

5.2.1 Evolution algorithms

The Evolution algorithms are natural evolution based search methods, which mimic biological evolution processes (the natural selection). The basic idea is that the environmental pressure causes the natural selection in given population of individuals. The fittest individuals will survive [13]. In case of material parameter calibration are individuals represented by a set of material model parameters and fitness is represented by the objective function. Evolution algorithms can be described using simple diagram, which is shown in Figure 5.4.

Initialisation is the first step of an evolution algorithm, when the initial population is chosen. Each iteration (generation) of evolution algorithm consists of parents selection, recombination, mutation, evaluation of the offspring fitness and selection from the fittest survivors. Recombination and mutation drives the diversity of the population and survivor selection provides the quality of population. The difference between recombination and mutation is the number of parents. During recombination, a one new offspring is created from two or more parents. Mutation creates a new offspring from one parent [13]. The termination condition is often the number of performed iterations (generations).

Evolution algorithm was used as the starting algorithm for the material parameters calibration, which should find the initial parameters of given material models. OptiSLang uses advanced evolution algorithms, which can combine more searching strategies at once. There is a large number of parameters of the evolution algorithm in optiSLang. New version of optiSLang has predefined settings for global and local optimisations. These settings were used during material parameter calibration. As the initial parameters of evolution algorithms, the following has to be set: the initial material parameters and their boundaries, starting population size, archive size and minimum and maximum number of generations. The rest of the evolution algorithm parameters are set by choosing predefined settings. As an initial population, the Latin hypercube Sampling is used. More information about the used evolution algorithm can be found in optiSLang documentation [3].

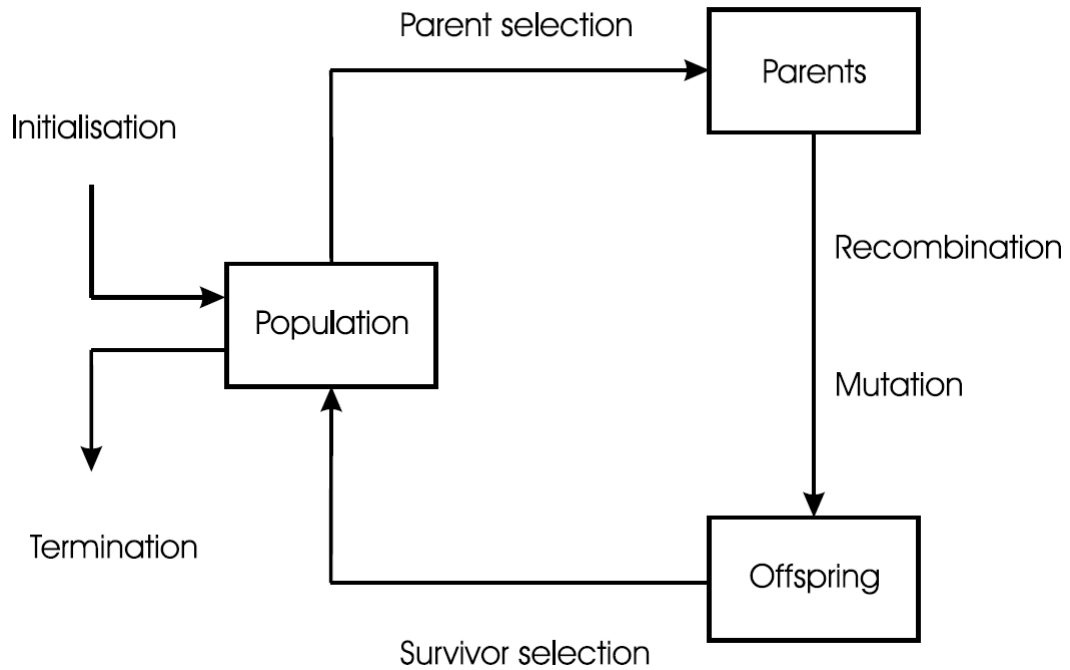


Figure 5.4: Scheme of evolution algorithms [13]

5.2.2 Gradient based algorithm

Nonlinear Programming by Quadratic Lagrangian (NLPQL) is a gradient-based local single objective optimisation algorithm. The objective function is internally approximated by a quadratic Taylor series, taking into consideration the estimated second-order derivatives from previous iteration steps. The NLPQL method is suitable for local optimisation with up to 20 variables. Local minimum is searched around the initial set of parameters. The initial parameters of NLPQL method are: the initial material parameters and their boundaries, desired accuracy, differentiation scheme, differentiation step size and others. Further details of the method can be found in [3]. This algorithm was used to refine material parameters calibrated using the evolution algorithm.

5.3 Objective function

To express the difference between experimental and model predicted data, the objective (error) function f must be defined. The error prediction can be expressed as [9]:

$$error = f(\mathbf{y}^{\text{pred}} - \mathbf{y}^{\text{exp}}), \quad (5.2)$$

where \mathbf{y}^{exp} is the vector of experimental data and \mathbf{y}^{pred} is the vector of predicted data, *error* is the scalar value and f is an objective function, which can be expressed in many different ways. In this thesis, the objective function was chosen in the following form:

$$f(\mathbf{y}^{\text{exp}}, \mathbf{y}^{\text{pred}}) = \frac{1}{N} \sum_{i=1}^N \frac{\sqrt{(y_i^{\text{exp}} - y_i^{\text{pred}})^2}}{\left(\sqrt{y_i^{\text{exp}}}\right)^2}, \quad (5.3)$$

where N is the total number of compared points and i is the position in the vector of experimental or predicted data. y_i^{exp} is the experimental value at i th position of \mathbf{y}^{exp} and y_i^{pred} is the predicted value at i th position of $\mathbf{y}^{\text{model}}$.

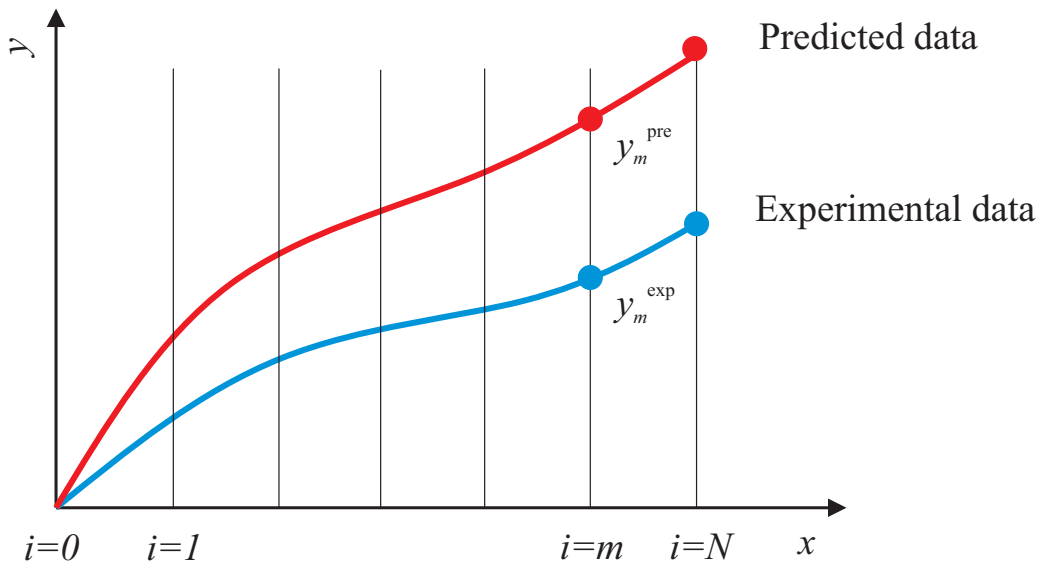


Figure 5.5: Comparison of predicted and experimental data

The objective function used in this thesis is defined in terms of force-time dependence, where predicted force and experimental force are compared as shown in Figure 5.6. Experimental and predicted values are interpolated using linear interpolation to obtain two vectors of the same length. For these vectors, the particular objective function can be evaluated in form:

$$f(\mathbf{F}^{\text{exp}}, \mathbf{F}^{\text{pred}}) = \frac{1}{N} \sum_{i=1}^N \frac{\sqrt{(F_i^{\text{exp}} - F_i^{\text{pred}})^2}}{\left(\sqrt{F_i^{\text{exp}}}\right)^2}, \quad (5.4)$$

where \mathbf{F}^{exp} is the vector of interpolated experimental force and \mathbf{F}^{pred} is the vector of interpolated predicted force. F_i are elements of vectors and N is the total number of compared points.

In order to achieve better results, the modified objective function 5.4 was used. Additional weight was added to the relaxation parts. Modified objective function has the form:

$$\bar{f} = f(\mathbf{F}^{\text{exp}}, \mathbf{F}^{\text{pred}}) + wf(\mathbf{F}_{\text{relax}}^{\text{exp}}, \mathbf{F}_{\text{relax}}^{\text{pred}}), \quad (5.5)$$

where $\mathbf{F}_{\text{relax}}$ are vectors of interpolated forces belonging to the relaxation parts of models/experiments and w is the weight coefficient. Relaxation parts of experiments are highlighted in Figure 5.6.

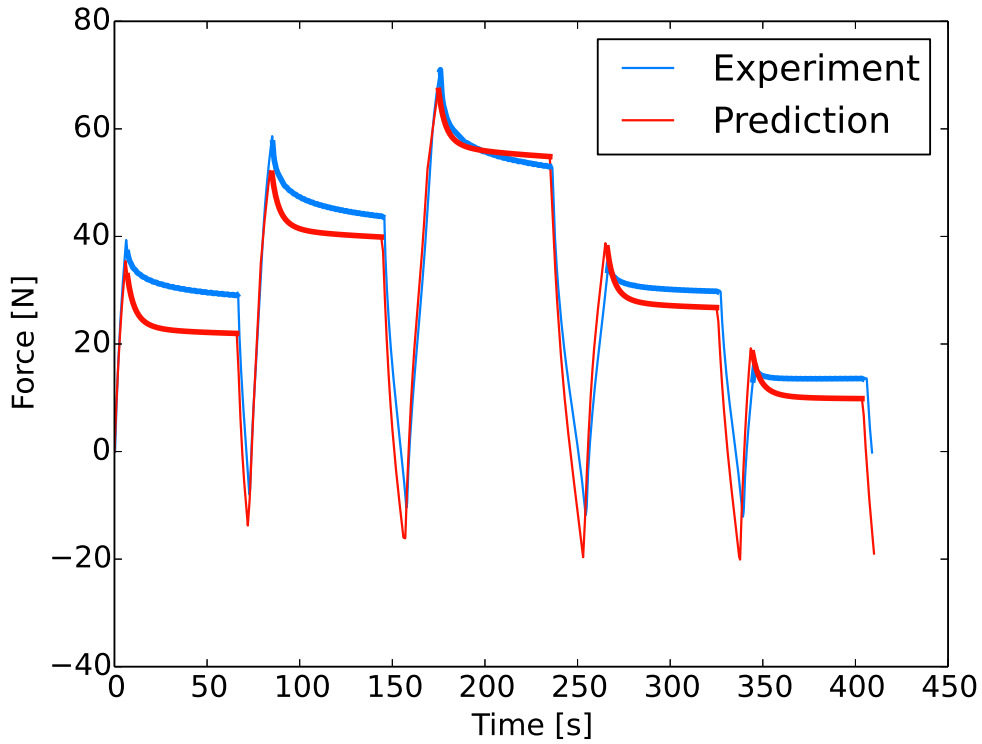


Figure 5.6: Time-force diagram with relaxation parts highlighted

Experiments were performed for different strain rates and loading modes. In order to identify parameters which satisfy all of the investigated strain rates and loading modes, the total objective function f_{total} must be defined. This function is defined as a sum of particular objective functions for given strain rate and loading mode as:

$$f_{\text{total}} = \sum_{\text{srates}} \sum_{\text{modes}} \bar{f}(\mathbf{F}_{\text{srate, mode}}^{\text{exp}}, \mathbf{F}_{\text{srate, mode}}^{\text{pred}}), \quad (5.6)$$

where $\mathbf{F}_{\text{srate, mode}}$ are vectors of interpolated forces for given strain rate and loading mode.

5.4 Optimization task

The optimisation task was developed as an universal tool for material parameters calibration. This task uses Abaqus as a solver, optiSLang as an optimisation software and Python scripts to connect it all together. Figure 5.7 shows the diagram of the optimisation task.

This task allows us to calibrate material parameters of random rubber-like material if the experimental data in uniaxial tension, uniaxial compression and simple shear are available. Finite element models are fully parametrical, loading history can be set using tabular data and number of investigated strain rates is not limited. Inputs of this task are parameters of optimisation algorithm, initial material parameters with boundaries and parameters of performed experiments (dimensions, strain rates, loading history, loading modes).

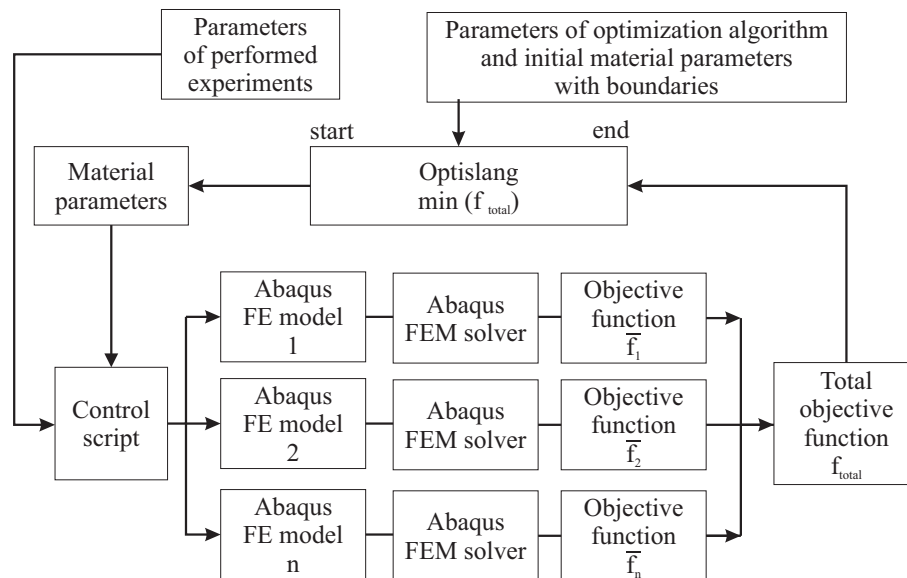


Figure 5.7: Diagram of the optimisation task

5.5 Cork-rubber parameters calibration

The material parameter calibration of the cork-rubber composite was performed using experimental data, numerical simulations and optimisation task mentioned in the previous section. The parameters were calibrated in order to describe the behaviour of the material in given loading modes and different strain rates. The material parameters calibration for given combination of loading modes and strain rates means that the optimisation task

consists of all combinations of given loading modes and given strain rates. The total objective function is the sum of particular objective functions.

It was originally planned to calibrate all 18 material parameters for a combination of three loading modes (uniaxial tension, uniaxial compression, simple shear) and three strain rates 0.01s^{-1} , 0.1s^{-1} and 1s^{-1} in order to predict complex behaviour of the cork composite. This calibration was unsuccessful and suitable parameters were not found. The biggest problem was caused by the numerical simulation of uniaxial compression, which is unstable for most material parameter combinations. Figure 5.8 (a), (b) shows results of numerical simulation for coarse and fine mesh with 20% nominal strain. It can be observed that the outer elements which are in the contact with rigid parts are excessively distorted. A large number of simulations did not converge during the optimisation.

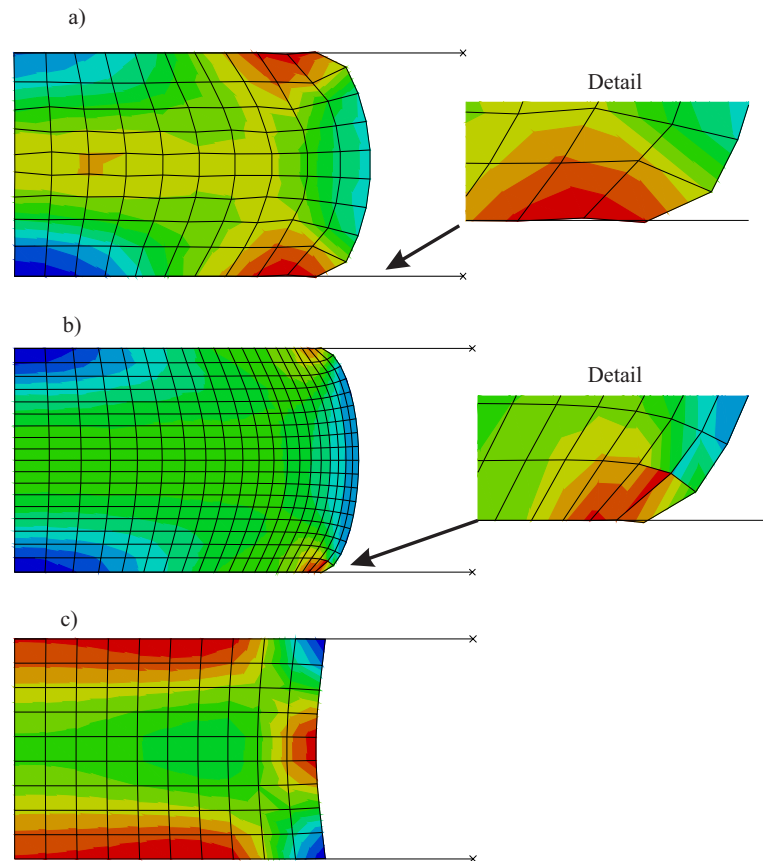


Figure 5.8: Uniaxial compression simulation errors

Other problems were caused by compressibility of the hyperelastic material model, where parameter D larger than $1 \times 10^{-7} [\text{Nm}^{-2}]$ caused bulging of compression sample model in the opposite direction as shown in Figure 5.8 (c). Parameter D of Arruda-Boyce hyperelastic model should correspond with $1/K_0 = 9.3 \times 10^{-6} [\text{Nm}^{-2}]$, however for these values the opposite bulging appears. This behaviour can not be seen in force-time

or force-displacement diagram, nor objective function can not register this behaviour. Only in the results visualization can this behaviour be observed. For a proper material calibration should be parameters for which the opposite bulging appears penalised in terms of objective function.

5.5.1 Calibration for combination of tension and shear

Due to the problems with numerical simulations of uniaxial compression, the material parameter calibration was only done for the combination of uniaxial tension, simple shear and all of the strain rates listed above. The calibration consisted of 3 steps where the evolution algorithm with global and local predefined settings was used to calibrate the material parameters, and these parameters were refined using the gradient algorithm as shown in Figure 5.9. The following procedure of material parameters calibration showed to be the most feasible way of finding proper parameters. Series of material parameter calibration with various parameters preceded this procedure in order to find initial values, boundaries and parameters of numerical optimization algorithms.

Calibration

The inputs of the global evolution algorithm were the initial parameters and boundaries listed in Table 5.2. As a simplification of the material model were the parameters n_i and m_i set constant to provide linear viscoelastic response of the particular network. It was less complicated to calibrate material parameters for linear version of the model first and then calibrate parameters which cause non-linear viscoelastic response. Based on the initial results of the calibration, it was preferable to assume the material to be incompressible ($D = 0$), although the value of the initial bulk modulus K_0 corresponds to compressible material. This assumption might be incorrect in case of uniaxial compression simulation, but it led to better results for the combination of tension and shear.

The best results of the global evolution algorithm were used as the initial values of the local evolution algorithm, but parameters n_i and m_i were no longer constant in order to provide non-linear viscoelastic response of a particular network. The initial parameters and boundaries of the local evolution algorithm are listed in 5.3. At the end, the gradient algorithm was used to refine parameters calibrated using the evolution algorithms. The initial parameter belonged to the best calibrated set of parameters from local evolution algorithm and boundaries were identical to the local evolution algorithm (Table 5.3).

Table 5.2: Parameters with initial values and boundaries for the global evolution algorithm

Parameter	Units	Initial value	Lower bound	Upper bound
μ	Nm^{-2}	0.75×10^6	0.5×10^6	2.5×10^6
λ	-	1	1	10
D	N^{-1}m^2	0	constant	constant
A_1	$\text{N}^{-n}\text{m}^{2n_s(-1-m)}$	1×10^{-6}	1×10^{-2}	1×10^{-14}
n_1	-	1	constant	constant
m_1	-	0	constant	constant
s_1	-	0.2	0	0.5
A_2	$\text{N}^{-n}\text{m}^{2n_s(-1-m)}$	1×10^{-6}	1×10^{-2}	1×10^{-14}
n_2	-	1	constant	constant
m_2	-	0	constant	constant
s_2	-	0.2	0	0.5
A_3	$\text{N}^{-n}\text{m}^{2n_s(-1-m)}$	1×10^{-6}	1×10^{-2}	1×10^{-14}
n_3	-	1	constant	constant
m_3	-	0	constant	constant
s_3	-	0.2	0	0.5
r	-	1	1	10
m	J	0.5	0.001	0.5
β	-	0.5	0	1

Table 5.3: Parameters with initial values and boundaries for the local evolution and gradient algorithm

Parameter	Units	Initial value	Lower bound	Upper bound
μ	Nm^{-2}	from previous algorithm	0.5×10^6	2.5×10^6
λ	-	from previous algorithm	1	10
D	N^{-1}m^2	0	constant	constant
A_1	$\text{N}^{-n}\text{m}^{2n_s(-1-m)}$	from previous algorithm	1×10^{-2}	1×10^{-14}
n_1	-	1	1	5
m_1	-	0	0	-1
s_1	-	from previous algorithm	0	0.5
A_2	$\text{N}^{-n}\text{m}^{2n_s(-1-m)}$	from previous algorithm	1×10^{-2}	1×10^{-14}
n_2	-	1	1	5
m_2	-	0	0	-1
s_2	-	from previous algorithm	0	0.5
A_3	$\text{N}^{-n}\text{m}^{2n_s(-1-m)}$	from previous algorithm	1×10^{-2}	1×10^{-14}
n_3	-	1	1	5
m_3	-	0	0	-1
s_3	-	from previous algorithm	0	0.5
r	-	from previous algorithm	1	10
m	J	from previous algorithm	0.001	0.5
β	-	from previous algorithm	0	1

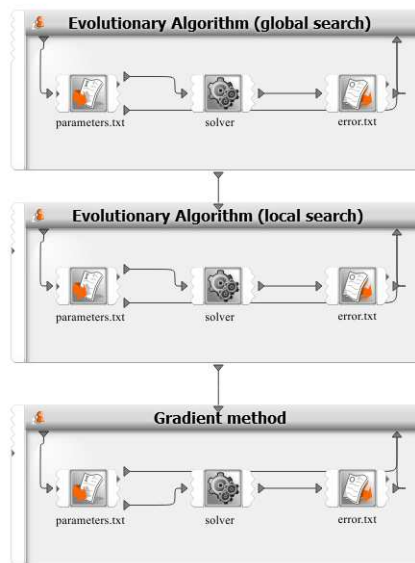


Figure 5.9: Scheme of the optimisation procedure

Algorithms parameters

As mentioned previously, evolution algorithms used predefined global or local search settings, which set the parameters of mutation, combination and other aspects. The basic parameters of the algorithm used during the calibration are listed in Table 5.4.

In order to satisfy the relation (4.46), the constraint for the stiffness of viscoelastic networks was used in form:

$$\sum_{i=1}^n s_i \leq 1 \quad (5.7)$$

Table 5.4: Parameters of algorithms

Parameter	Algorithm	Value
Start population size	Global e.	2000
Archive size	Global e.	100
Maximum number of generations	Global e.	3
Start population size	Local e.	50
Archive size	Local e.	5
Maximum number of generations	Local e.	100
Desired accuracy	Gradient	0.5×10^{-6}
Differentiation scheme	Gradient	central
Differentiation step size	Gradient	0.001
Maximum num. of solver runs	Gradient	10000

6 Results

Based on the initial results of material parameter calibration and problems with convergence of uniaxial compression were material parameters calibrated only for the combination of uniaxial tension and simple shear. Incompressible material was assumed.

The following Figures 6.1 - 6.12 show the results of experiments and numerical predictions for calibrated material parameters listed in Table 6.1. For calibrated material parameters, a compliance between predictions and experiments was achieved, however the predictions of uniaxial tension are less stiff than the experiments. The situation is opposite in case of simple shear, the predictions are stiffer than the experiments. From the force-time diagrams it is obvious that the relaxation parts are not predicted well, the decrease of reaction force in predictions is smaller than the measured force. The biggest calibration errors of approximately 30 % can be found in the relaxation parts. The calibrated material models correspond to slightly non-linear viscoelastic model because of parameters m_i and n_i , whose values are equal or almost equal to values corresponding with the linear model. This is caused by the procedure of material parameters calibration which started with linear version of the model.

Figures 6.13-6.18 show the results of experiments and predictions of uniaxial compression. It is obvious that the material parameters calibrated for tension and shear are not suitable for uniaxial compression. The predictions are much stiffer than the experiments. In addition, the results for strain rate 0.1 s^{-1} (Figures 6.15 and 6.16) are not complete, only half of the simulation is completed. For this simulation, the mesh shown in Figure 5.2 (a) was used.

Material parameters calibrated in this thesis are appropriate for predicting the behaviour of the cork-rubber composite in case of tension or shear loading for strain rates 0.01 s^{-1} , 0.1 s^{-1} , 1 s^{-1} . It can be assumed that for other strain rates close to previously mentioned ones will the material model with given parameters be accurate enough. Material parameters were calibrated for relaxation time 60 s, for longer relaxation times are the calibrated parameters not suitable. This material model will predict the behaviour of the material under cyclic loading for strains up to 30% because of Mullins effect.

Table 6.1: Results of material parameter calibration for combination of tension and shear

Parameter	Units	Value
μ	Nm^{-2}	1141655
λ	-	4.0952
d	N^{-1}m^2	0
A_1	$\text{N}^{-n}\text{m}^{2n}\text{s}^{(-1-m)}$	1.86×10^{-9}
n_1	-	1
m_1	-	0
s_1	-	0.0775
A_2	$\text{N}^{-n}\text{m}^{2n}\text{s}^{(-1-m)}$	1.12×10^{-9}
n_2	-	1.3028
m_2	-	0
s_2	-	0.4682
A_3	$\text{N}^{-n}\text{m}^{2n}\text{s}^{(-1-m)}$	9.90×10^{-7}
n_3	-	1.2567
m_3	-	0
s_3	-	0.1865
r	-	1.5810
m	J	0.3787
β	-	1.0829

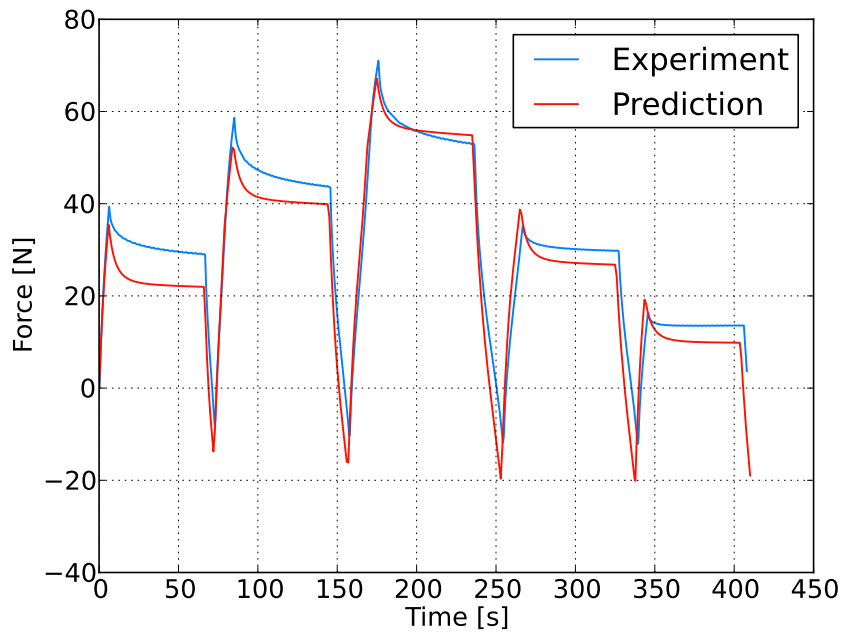


Figure 6.1: Comparison of experimental and predicted data for calibrated parameters: force-time diagram, uniaxial tension, strain rate 1 s^{-1} .

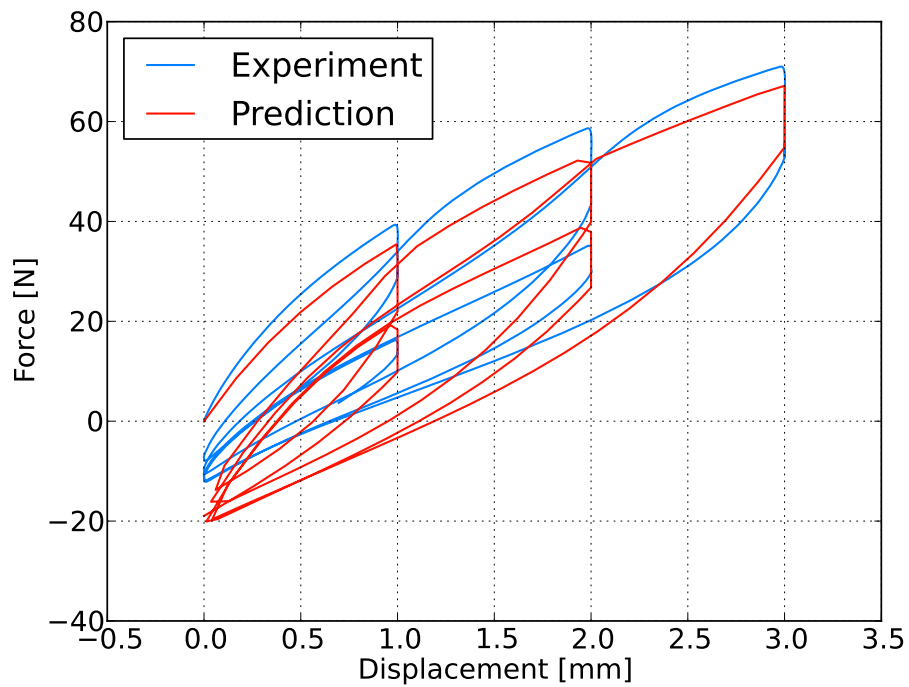


Figure 6.2: Comparison of experimental and predicted data for calibrated parameters: force-displacement diagram, uniaxial tension, strain rate 1 s^{-1} .

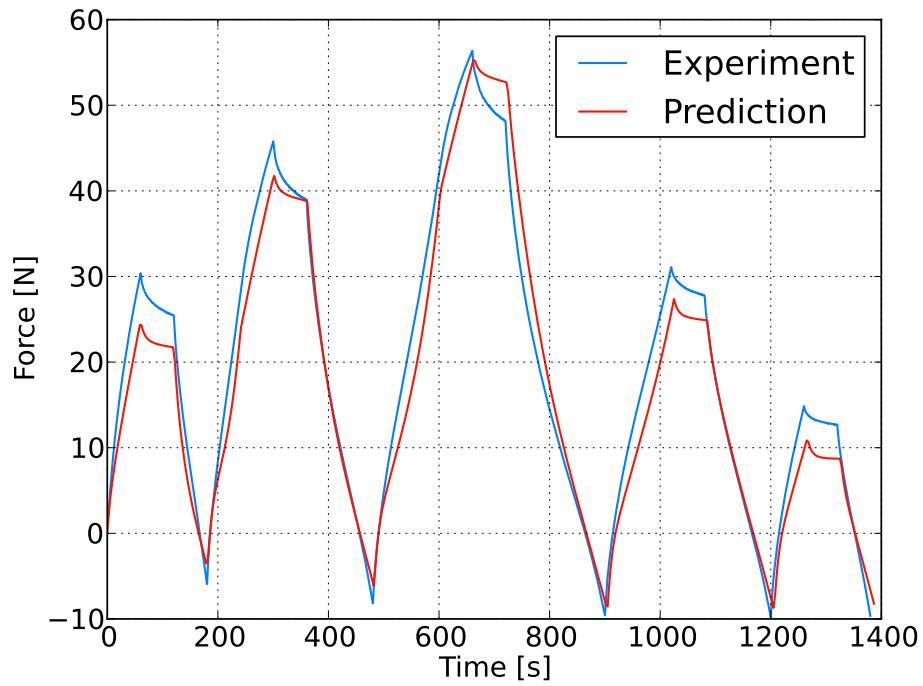


Figure 6.3: Comparison of experimental and predicted data for calibrated parameters: force-time diagram, uniaxial tension, strain rate 0.1 s^{-1} .

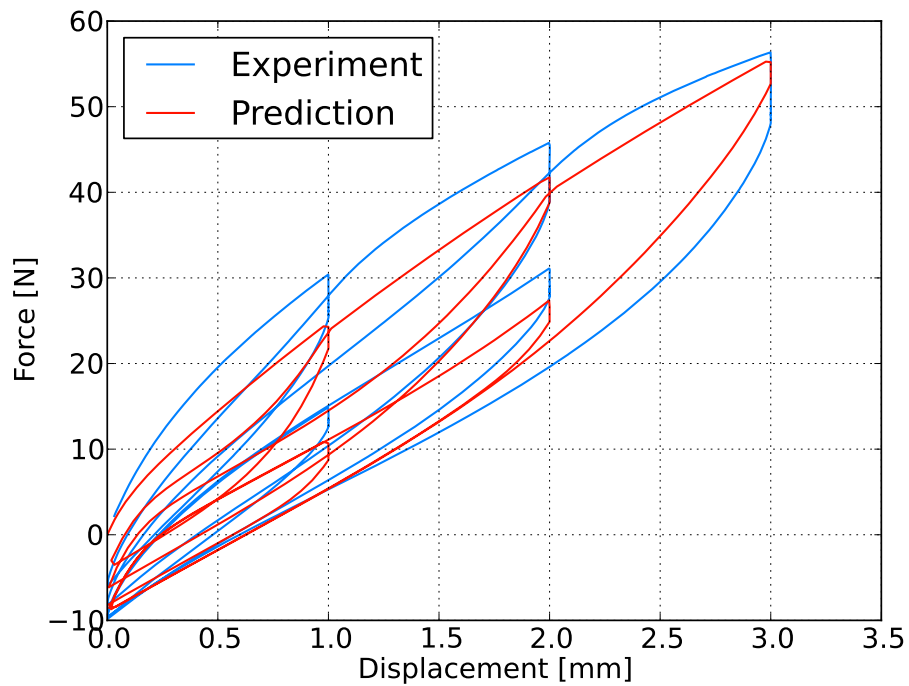


Figure 6.4: Comparison of experimental and predicted data for calibrated parameters: force-displacement diagram, uniaxial tension, strain rate 0.1 s^{-1} .

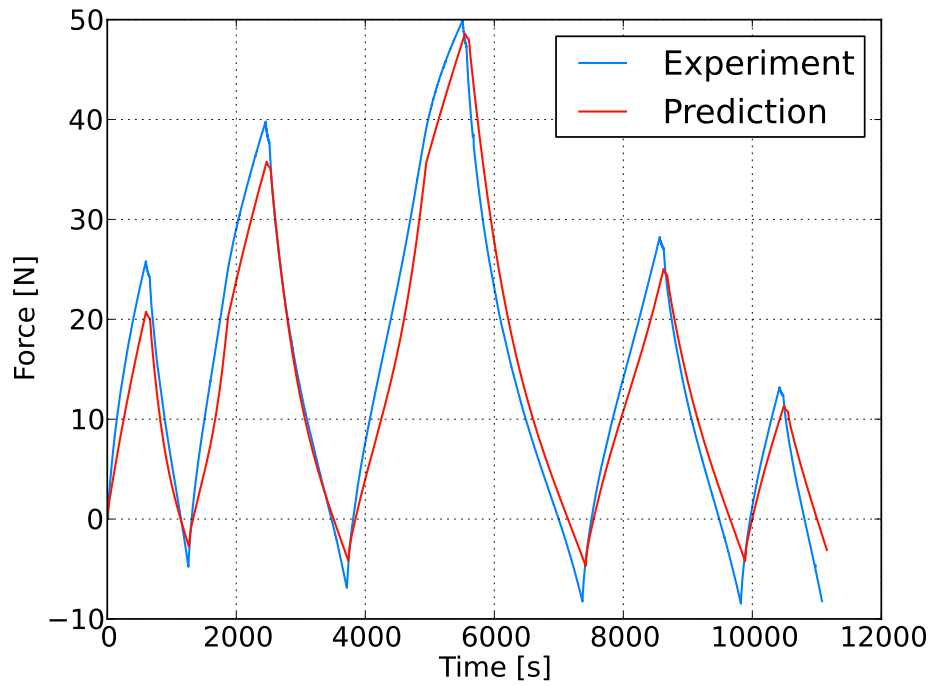


Figure 6.5: Comparison of experimental and predicted data for calibrated parameters: force-time diagram, uniaxial tension, strain rate 0.01 s^{-1} .

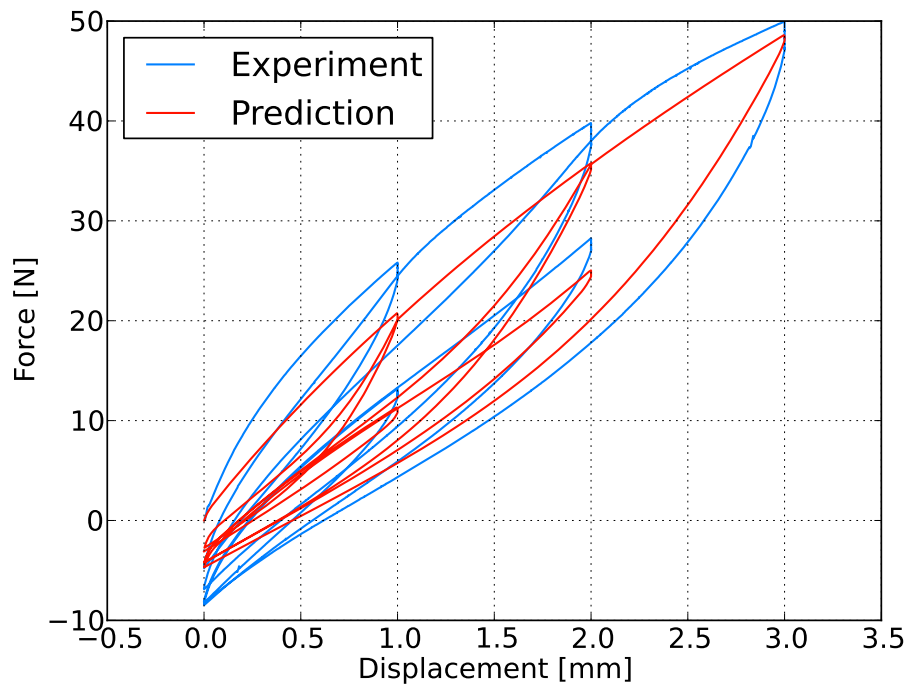


Figure 6.6: Comparison of experimental and predicted data for calibrated parameters: force-displacement diagram, uniaxial tension, strain rate 0.01 s^{-1} .

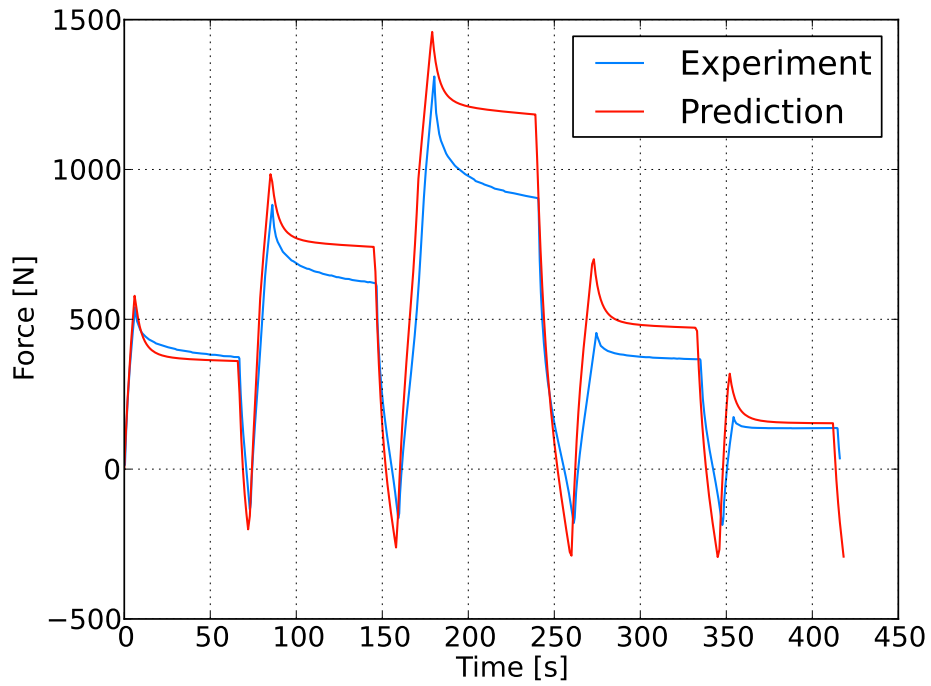


Figure 6.7: Comparison of experimental and predicted data for calibrated parameters: force-time diagram, simple shear, strain rate 1 s^{-1} .

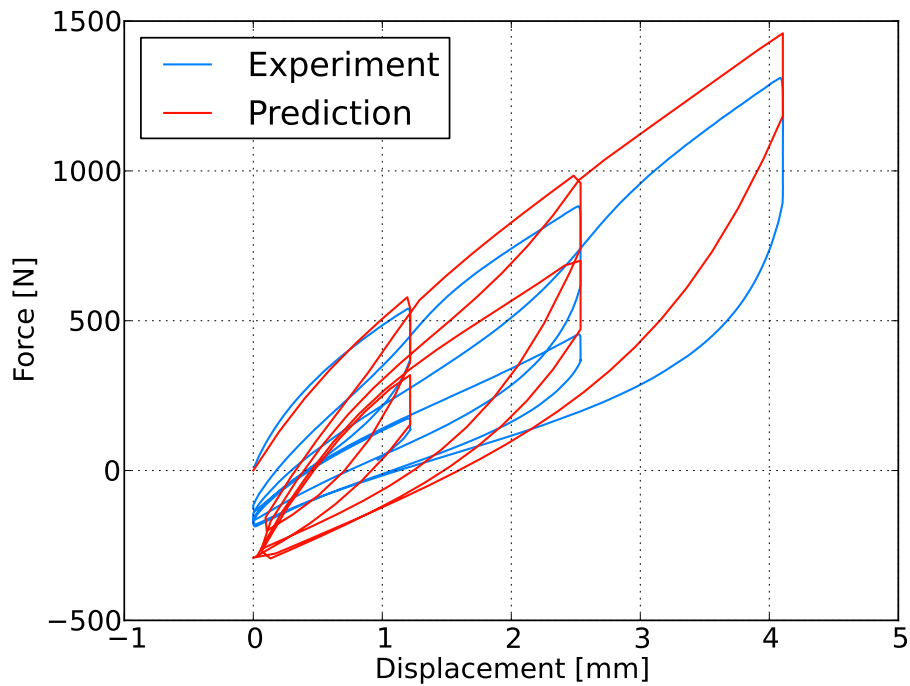


Figure 6.8: Comparison of experimental and predicted data for calibrated parameters: force-displacement diagram, simple shear, strain rate 1 s^{-1} .

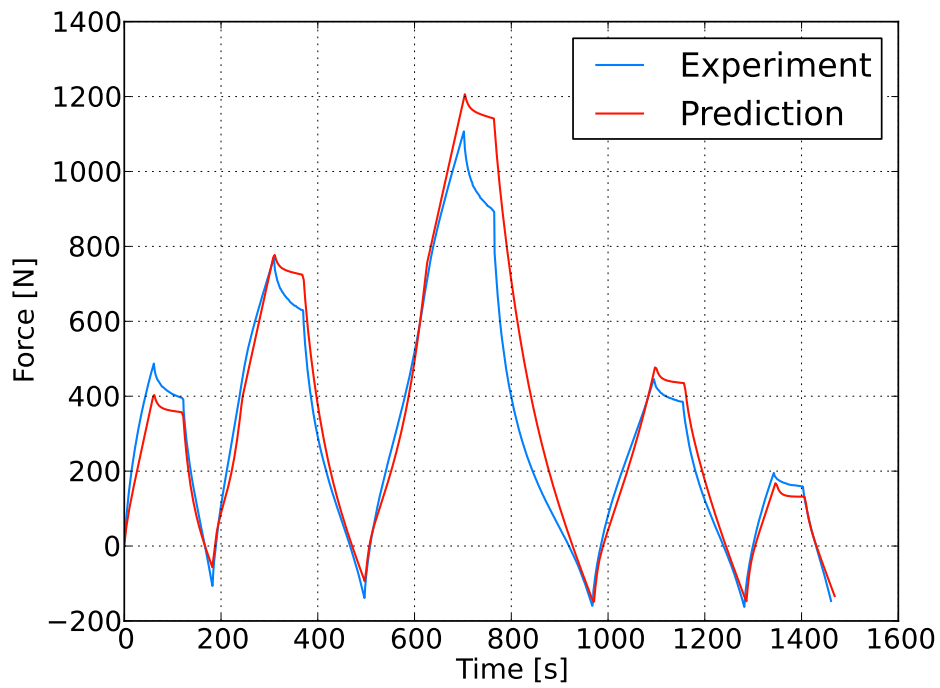


Figure 6.9: Comparison of experimental and predicted data for calibrated parameters: force-time diagram, simple shear, strain rate 0.1 s^{-1} .

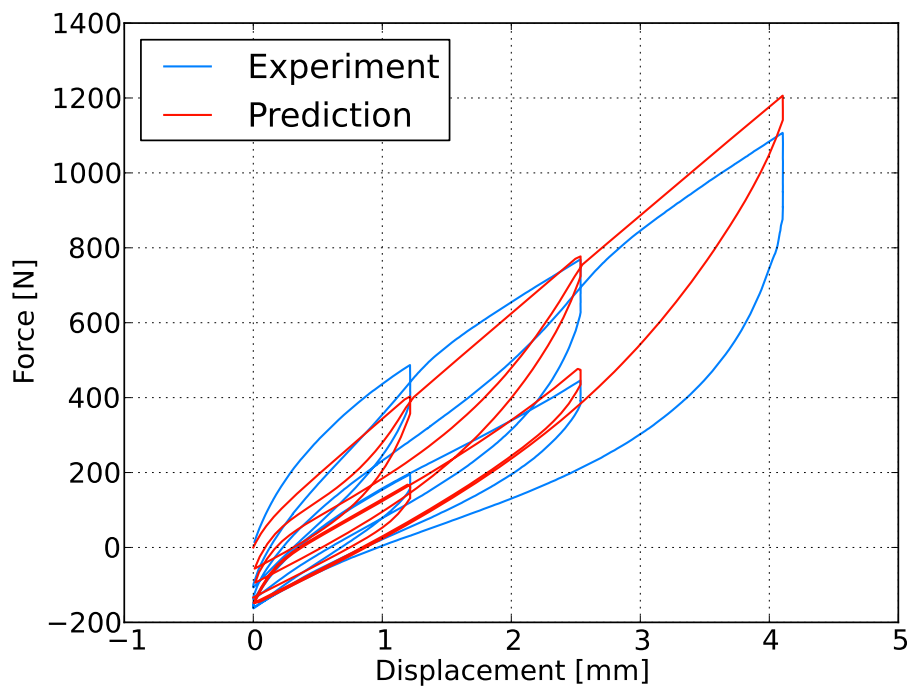


Figure 6.10: Comparison of experimental and predicted data for calibrated parameters: force-displacement diagram, simple shear, strain rate 0.1 s^{-1} .

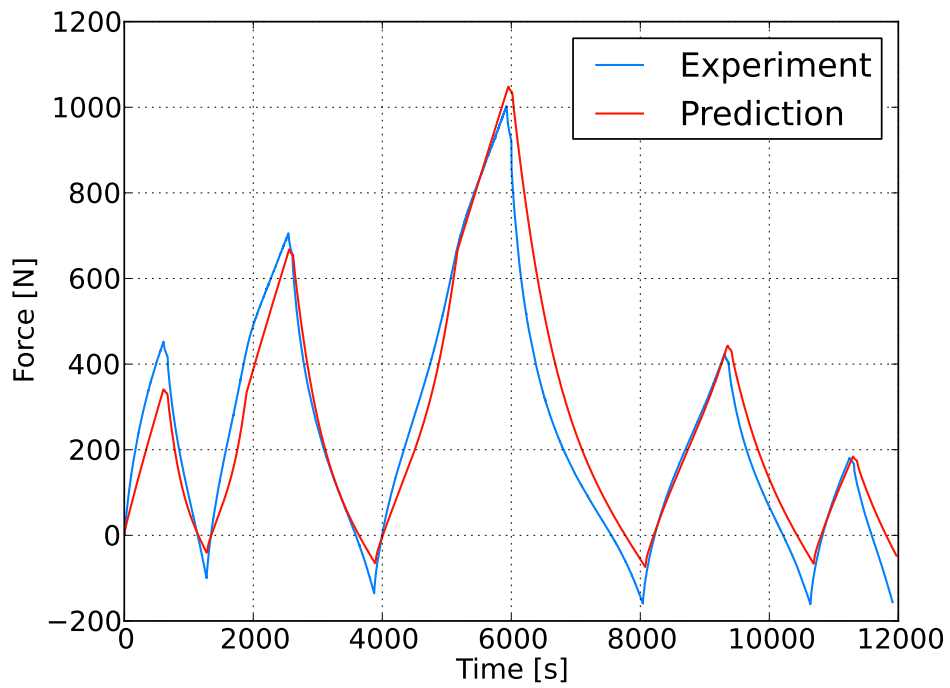


Figure 6.11: Comparison of experimental and predicted data for calibrated parameters: force-time diagram, simple shear, strain rate 0.01 s^{-1} .

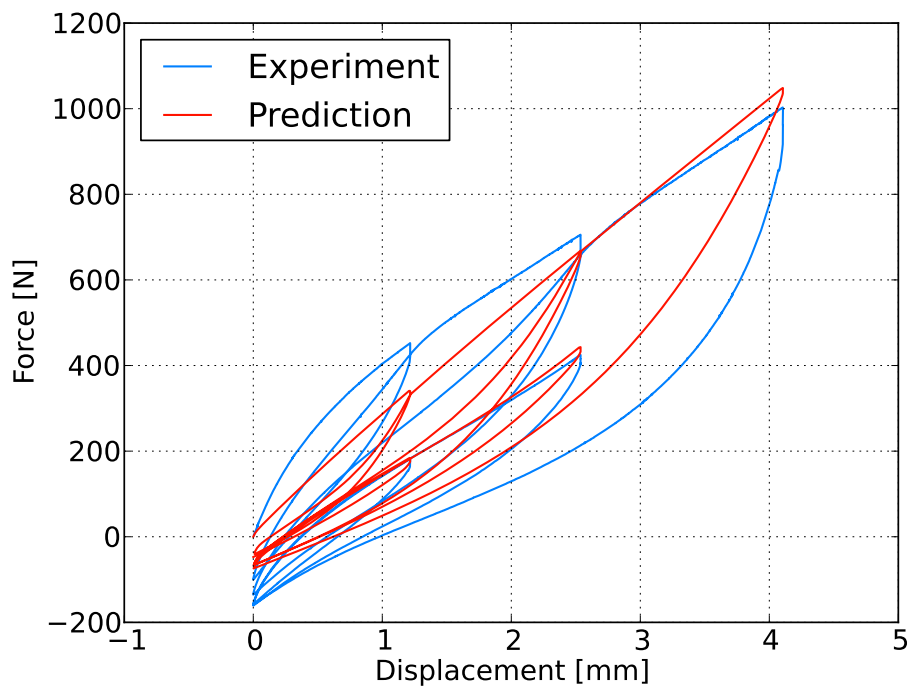


Figure 6.12: Comparison of experimental and predicted data for calibrated parameters: force-displacement diagram, simple shear, strain rate 0.01 s^{-1} .

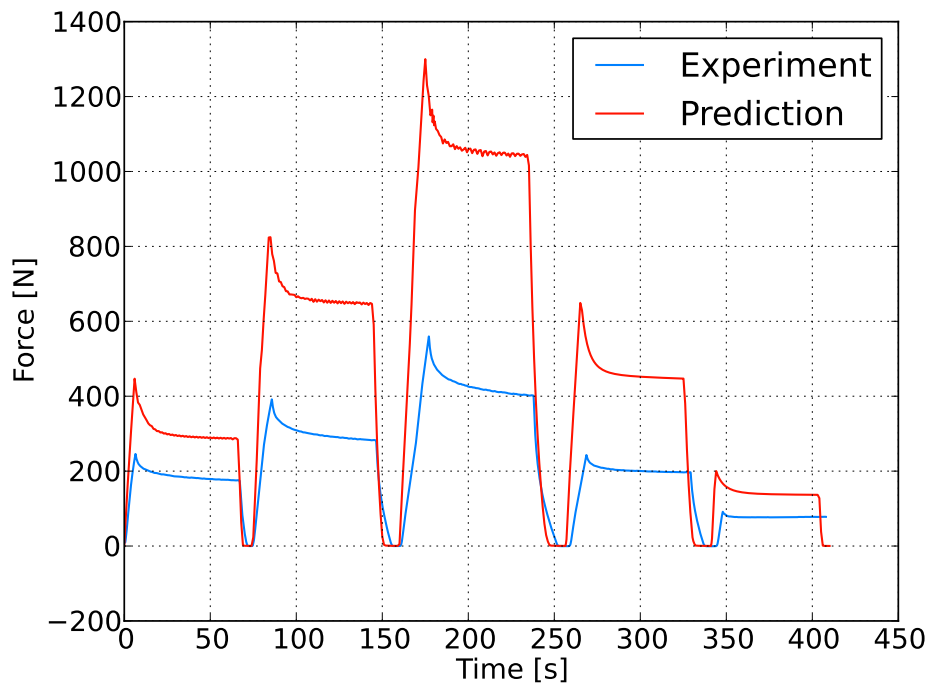


Figure 6.13: Comparison of experimental and predicted data for calibrated parameters: force-time diagram, uniaxial compression, strain rate 1 s^{-1} .

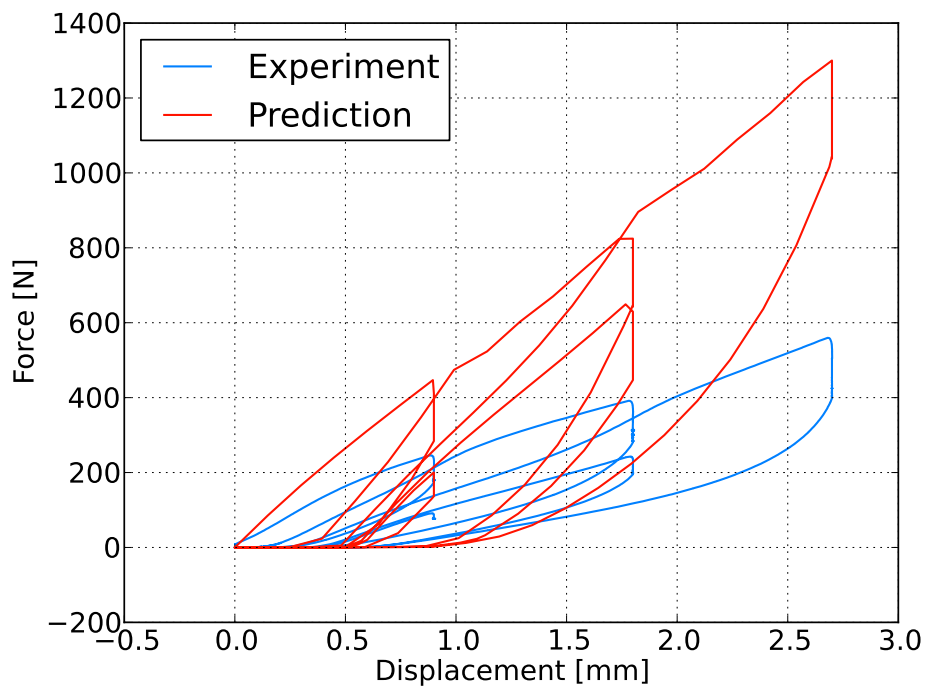


Figure 6.14: Comparison of experimental and predicted data for calibrated parameters: force-displacement diagram, uniaxial compression, strain rate 1 s^{-1} .

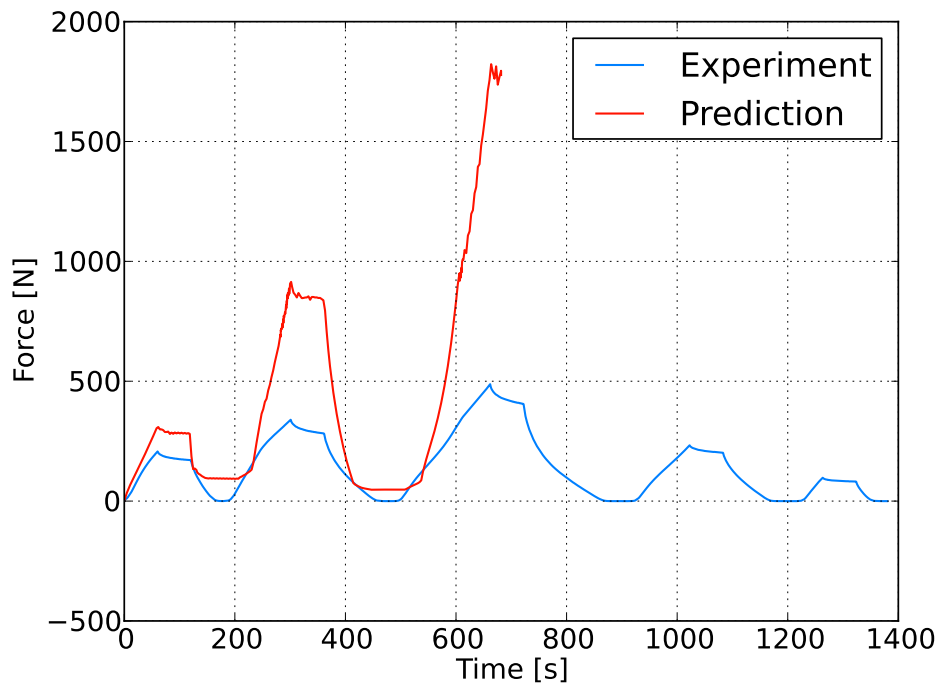


Figure 6.15: Comparison of experimental and predicted data for calibrated parameters: force-time diagram, uniaxial compression, strain rate 0.1 s^{-1} .

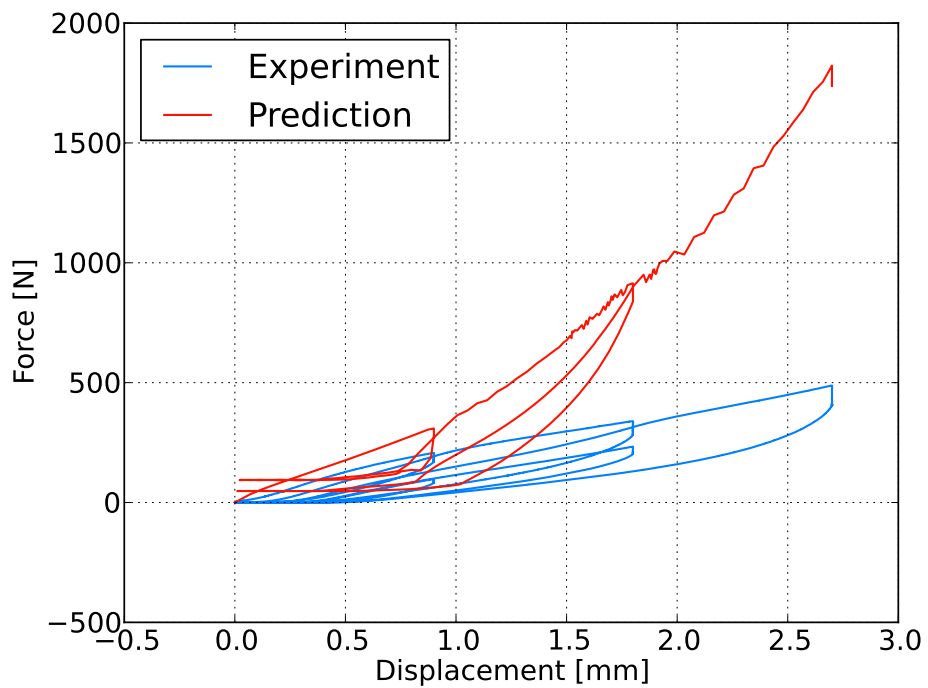


Figure 6.16: Comparison of experimental and predicted data for calibrated parameters: force-displacement diagram, uniaxial compression, strain rate 0.1 s^{-1} .

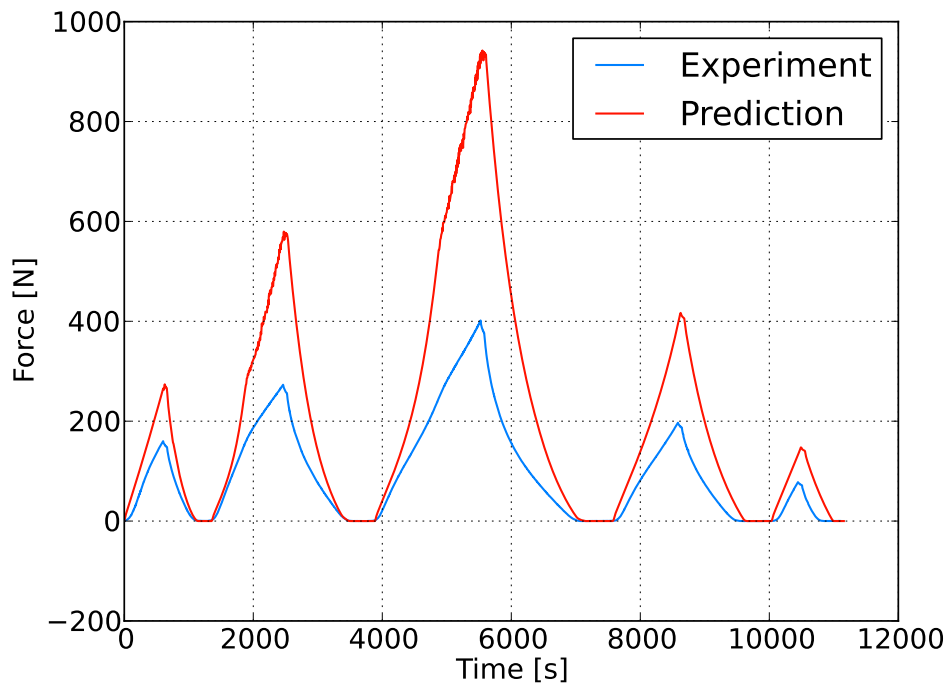


Figure 6.17: Comparison of experimental and predicted data for calibrated parameters: force-time diagram, uniaxial compression, strain rate 0.01 s^{-1} .

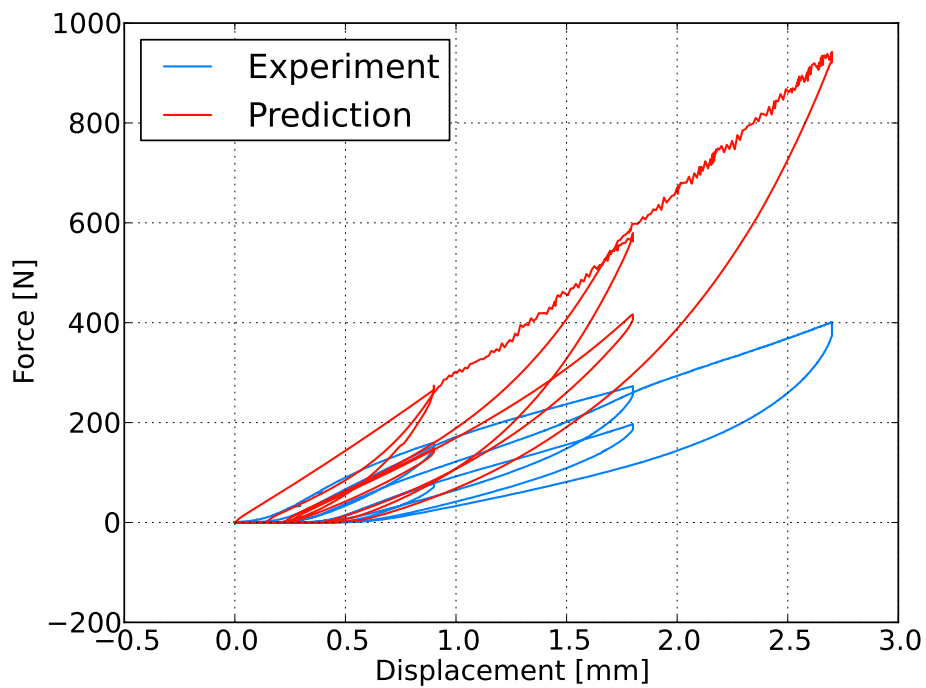


Figure 6.18: Comparison of experimental and predicted data for calibrated parameters: force-displacement diagram, uniaxial compression, strain rate 0.01 s^{-1} .

7 Conclusion

The presented diploma thesis dealt with cork-rubber material parameter calibration. Uniaxial tension, uniaxial compression and simple shear experiments were performed for strain rates 0.01s^{-1} , 0.1s^{-1} , 1s^{-1} in order to identify the behaviour of a cork-composite Amorim ACM87. As a material model was chosen the Parallel network model consisting of 3 viscoelastic networks in combination with Mullins effect. Viscoelastic networks were represented using hyperelastic Arruda-Boyce model and viscous Power law. Material parameters were calibrated using evolution and gradient algorithms driven by optiSLang software. Calibration was based on a comparison and minimization of the differences between experimental data and the results of numerical simulations. Numerical simulations corresponding with the experiments were performed using Abaqus software.

Due to problems with convergence of numerical simulations of uniaxial compression, only material parameters for combination of uniaxial tension and simple shear were calibrated, assuming incompressible material. Calibrated material parameters are suitable for describing the behaviour of the cork-rubber composite in case of tension and shear loading up to 30% nominal strains in range of strain rates from 0.01s^{-1} to 1s^{-1} . Investigated relaxation time was 60 s, for longer relaxation time will the predictions become more inaccurate.

The parameters of chosen material model were calibrated, however not for a combination of all loading modes. In further work, the problems with convergence of numerical simulations of uniaxial compression should be solved. Another possibility is to omit uniaxial compression and investigate other loading modes such as biaxial extension to avoid contact type numerical simulations. Also other hyperelastic models and viscous laws should be investigated in order to find better compliance between the experiments and numerical simulation predictions.

Bibliography

- [1] Abaqus 6.14 analysis user's guide.
- [2] Mechanics of elastic solids. <https://www.brown.edu/Departments/Engineering/Courses/En221/Notes/Elasticity/Elasticity.htm>. [Online; accessed 1-May-2016].
- [3] Optislang 4.2 documentation.
- [4] Veryst engineering, polymer modeling. <http://www.veryst.com/what-we-offer/polymer-modeling>. [Online; accessed 1-May-2016].
- [5] ASTM Standard D575 – 91. “Standard Test Methods for Rubber Properties in Compression”. West Conshohocken, PA, 2012.
- [6] E. M. Arruda and M. C. Boyce. A three-dimensional constitutive model for the large stretch behavior of rubber elastic materials. *Journal of the Mechanics and Physics of Solids*, 41(2):389 – 412, 1993.
- [7] J. Bergström. Constitutive modeling of elastomers – accuracy of predictions and numerical efficiency. <https://polymerfem.com/>. [Online; accessed 1-May-2016].
- [8] J. Bergström. Material models. <https://polymerfem.com/content.php?71-material-models>. [Online; accessed 1-May-2016].
- [9] J. Bergström. *Mechanics of Solid Polymers - Theory and Computational Modeling*. Elsevier Science and Technology Books, Oxford, 2015.
- [10] R. Brown. *Physical testing of rubber*. Springer, New York, 2006.
- [11] T . Dalrymple, J . A . Hurtado, I . Lapczyk, and H . R . Ahmadi. Parallel rheological framework to model the amplitude dependence of the dynamic stiffness in carbon-black filled rubber. *Constitutive Models for Rubbers IX*, 2015.
- [12] J. Diani, B. Fayolle, and P. Gilormini. A review on the mullins effect. *European Polymer Journal*, 45(3):601 – 612, 2009.
- [13] A. Eiben. *Introduction to evolutionary computing*. Springer, New York, 2003.

- [14] M. H. R. Ghoreishy. Determination of the parameters of the prony series in hyper-viscoelastic material models using the finite element method. *Materials and Design*, 35:791 – 797, 2012.
- [15] L. Gil. Cork composites: A review. *Materials*, 2(3):776, 2009.
- [16] L. Horný. Patobiomechanika srdečněcévního systému 1.díl. <http://users.fs.cvut.cz/hornyluk/home>. [Online; accessed 1-May-2016].
- [17] W. Hosford. *Solid Mechanics* -. Cambridge University Press, Cambridge, 2010.
- [18] J.A. Hurtado and I. Lapczyk. Parallel rheological framework to model non-linear viscoelasticity, permanent set, and mullins effect in elastomers. *Constitutive Models for Rubber VIII*, 2013.
- [19] M. Itskov. *Tensor Algebra and Tensor Analysis for Engineers - With Applications to Continuum Mechanics*. Springer Science and Business Media, Berlin Heidelberg, 2009.
- [20] P. Kelly. Solid mechanics part iv: Material models in continuum solid mechanics. <http://homepages.engineering.auckland.ac.nz/~pkel015/SolidMechanicsBooks/index.html>. [Online; accessed 5-May-2016].
- [21] P. Kelly. Solid mechanics part iv: Material models in continuum solid mechanics. http://homepages.engineering.auckland.ac.nz/~pkel015/SolidMechanicsBooks/Part_I/BookSM_Part_I/10_Viscoelasticity/10_Viscoelasticity_01_Intro.pdf. [Online; accessed 1-May-2016].
- [22] J. Kocáb. Identifikace materiálových parametrů nelineárního modelu pro popsání mechanických vlastností korkového kompozitu, bachaleor thesis, 2014.
- [23] A. Kossa. Lecture notes of continuum mechanics. <http://www.mm.bme.hu/~kossa>. [Online; accessed 1-May-2016].
- [24] R. Kottner, R. Zemčík, and J. Vacík. Improvement of damping properties of carbon fibre reinforced laminated plastics using damping layers. *Materiali in tehnologije / Materials and technology*, 47(2), mar 2013.
- [25] B. Nandi, T. Dalrymple, J. Yao, and I. Lapczyk. Importance of capturing non-linear viscoelastic material behavior in tire rolling simulations. <https://www.3ds.com/fileadmin/PRODUCTS/SIMULIA/PDF/whitepapers/capturing-non-linear-viscoelastic-tire-rolling-simulation.pdf>. [Online; accessed 1-May-2016].

-
- [26] J. Nocedal and S. Wright. *Numerical Optimization* -. Springer Science and Business Media, Berlin Heidelberg, 1st. ed. 1999. corr. 2nd printing edition, 2006.
- [27] C. Novotný. Viskoelastica. <http://mechanika.fs.cvut.cz/content/files/PC/Viskoelastica.pdf>. [Online; accessed 1-May-2016].
- [28] R. W. Ogden and D. G. Roxburgh. A pseudo–elastic model for the mullins effect in filled rubber. *Proceedings of the Royal Society of London A: Mathematical, Physical and Engineering Sciences*, 455(1988):2861–2877, 1999.
- [29] H. Pereira. *Cork biology, production and uses*. Elsevier, Amsterdam London, 2007.